JAMES | Journal of Advances in Modeling Earth Systems

RESEARCH ARTICLE
10.1029/2022MS003518

Comparing Two Parameterizations for the Restratification Effect of Mesoscale Eddies in an Isopycnal Ocean Model

Nora Loose[1,2], Gustavo M. Marques[3], Alistair Adcroft[2], Scott Bachman[3], Stephen M. Griffies[2,4], Ian Grooms[1], Robert W. Hallberg[2,4], and Malte F. Jansen[5]

[1]Department of Applied Mathematics, University of Colorado, Boulder, CO, USA, [2]Atmospheric and Oceanic Sciences, Princeton University, Princeton, NJ, USA, [3]Climate and Global Dynamics Laboratory, National Center for Atmospheric Research, Boulder, CO, USA, [4]NOAA Geophysical Fluid Dynamics Laboratory, Princeton, NJ, USA, [5]Department of the Geophysical Sciences, The University of Chicago, Chicago, IL, USA

Abstract There are two distinct parameterizations for the restratification effect of mesoscale eddies: the Greatbatch and Lamb (1990, GL90, https://journals.ametsoc.org/view/journals/phoc/20/10/1520-0485_1990_020_1634_opvmom_2_0_co_2.xml?tab_body=abstract-display) parameterization, which mixes horizontal momentum in the vertical, and the Gent and McWilliams (1990, GM90, https://journals.ametsoc.org/view/journals/phoc/20/1/1520-0485_1990_020_0150_imiocm_2_0_co_2.xml) parameterization, which flattens isopycnals adiabatically. Even though these two parameterizations are effectively equivalent under the assumption of quasi-geostrophy, GL90 has been used much less than GM90, and exclusively in z-coordinate models. In this paper, we compare the GL90 and GM90 parameterizations in an idealized isopycnal coordinate model, both from a theoretical and practical perspective. From a theoretical perspective, GL90 is more attractive than GM90 for isopycnal coordinate models because GL90 provides an interpretation that is fully consistent with thickness-weighted isopycnal averaging, while GM90 cannot be entirely reconciled with any fully isopycnal averaging framework. From a practical perspective, the GL90 and GM90 parameterizations lead to extremely similar energy levels, flow and vertical structure, even though their energetic pathways are very different. The striking resemblance between the GL90 and GM90 simulations persists from non-eddying through eddy-permitting resolution. We conclude that GL90 is a promising alternative to GM90 for isopycnal coordinate models, where it is more consistent with theory, computationally more efficient, easier to implement, and numerically more stable. Assessing the applicability of GL90 in realistic global ocean simulations with hybrid coordinate schemes should be a priority for future work.

Plain Language Summary Ocean models are complex simulations run on large supercomputers, and are useful for predicting changes in ocean circulation and climate. Ocean models divide the globe into grid cells. Choosing many, very small grid cells is not feasible because the simulations would take too much time and would be too expensive. Therefore, the grid cells in most ocean models are not small enough to simulate mesoscale eddies. Mesoscale eddies are swirling motions that are less than 100 km wide and play an important role in transporting heat and carbon throughout the ocean. To still account for the effects of mesoscale eddies, one can use approximate "parameterizations." Which parameterization is "best" is an ongoing research question. This paper compares two parameterizations that simulate the effect of mesoscale eddies in two distinct ways: the commonly used Gent and McWilliams (1990, https://journals.ametsoc.org/view/journals/phoc/20/1/1520-0485_1990_020_0150_imiocm_2_0_co_2.xml) parameterization and the less commonly used Greatbatch and Lamb (1990, https://journals.ametsoc.org/view/journals/phoc/20/10/1520-0485_1990_020_1634_opvmom_2_0_co_2.xml?tab_body=abstract-display) parameterization. This paper shows that the two parameterizations impact ocean circulation in a very similar way, and that for a certain class of models the Greatbatch and Lamb (1990, https://journals.ametsoc.org/view/journals/phoc/20/10/1520-0485_1990_020_1634_opvmom_2_0_co_2.xml?tab_body=abstract-display) parameterization has advantages because it is more consistent with physical and mathematical theory, is easier to code, and leads to faster computations.

Key Points:

- We compare the Greatbatch and Lamb (1990, GL90, https://journals.ametsoc.org/view/journals/phoc/20/10/1520-0485_1990_020_1634_opvmom_2_0_co_2.xml?tab_body=abstract-display) and the Gent and McWilliams (1990, GM90, https://journals.ametsoc.org/view/journals/phoc/20/1/1520-0485_1990_020_0150_imiocm_2_0_co_2.xml) parameterizations in an isopycnal ocean model
- GL90 leads to very similar flow as GM90, for non-eddying through eddy-permitting resolution
- We argue, however, that for isopycnal coordinate models GL90 is more consistent with theory than GM90

Supporting Information:

Supporting Information may be found in the online version of this article.

Correspondence to:

N. Loose,
nora.loose@princeton.edu

Citation:

Loose, N., Marques, G. M., Adcroft, A., Bachman, S., Griffies, S. M., Grooms, I., et al. (2023). Comparing two parameterizations for the restratification effect of mesoscale eddies in an isopycnal ocean model. *Journal of Advances in Modeling Earth Systems*, *15*, e2022MS003518. https://doi.org/10.1029/2022MS003518

Received 9 NOV 2022
Accepted 6 NOV 2023

1. Introduction

The majority of oceanic kinetic energy (KE) is contained in the mesoscale eddy field, at horizontal scales of tens to hundreds of kilometers (Storer et al., 2022). Mesoscale eddies have a profound impact on the vertical structure

of the oceanic flow (de La Lama et al., 2016; Kjellsson & Zanna, 2017; Yankovsky et al., 2022). Eddy interfacial form stress, described by correlations between isopcynal interface displacements and pressure fluctuations, transfers horizontal momentum downward through layers of successively greater density (Johnson & Bryden, 1989). The role of interfacial form stress is perhaps most prominent in the Southern Ocean, where it mediates a governing momentum balance between the surface wind stress and topographic form stress across submarine ridges (Munk & Palmén, 1951; Rintoul et al., 2001).

Mesoscale eddies are not resolved in most of today's global ocean and climate models, and their effect on the larger-scale circulation and tracer transport needs to be parameterized. Greatbatch and Lamb (1990, hereafter GL90) and Greatbatch (1998) suggested that eddy interfacial form stress can be parameterized by a vertical eddy viscosity added to the model momentum equation. The GL90 scheme implies vertical mixing of geostrophic momentum, and acts as a sign-definite sink of KE. The GL90 vertical viscosity parameterization is consistent with a thickness-weighted average (TWA) framework (Young, 2012), in which the momentum equation solves for the isopycnal TWA velocity.

The TWA framework stands in contrast to the Eulerian mean and the isopycnal non-TWA frameworks. In the latter two frameworks, the model momentum equation solves only for the large-scale resolved velocity, while the eddy-induced velocity needs to be parameterized. The latter task is accomplished by the Gent and McWilliams (1990, hereafter GM90) scheme, with the eddy-induced velocity added to the model thickness and tracer equations. The GM90 parameterization mimics the effect of mesoscale eddies to adiabatically flatten isopycnals of large-scale currents, and acts as a sign-definite sink of available potential energy (APE) (Gent et al., 1995; Griffies, 1998). In spite of their formally different nature, the GL90 and GM90 parameterizations both mimic the restratification effect of mesoscale eddies. The two parameterizations can be linked via thermal wind balance: By flattening isopycnals, GM90 decreases horizontal density gradients, and thus reduces the vertical shear of the geostrophic flow. GL90 directly parameterizes the latter effect by mixing momentum in the vertical, with the baroclinicity adjusting via an ageostrophic flow. Moreover, by means of geostrophy, the GL90 vertical viscosity ν^{GL} can be cast in terms of the GM90 interface height diffusivity κ^{GM} as

$$\nu^{\mathrm{GL}} = \kappa^{\mathrm{GM}} f^2 / N^2, \tag{1}$$

where f is the Coriolis parameter and N the buoyancy frequency (McWilliams & Gent, 1994).

Even though born in the same year, the GM90 and GL90 schemes have enjoyed vastly different degrees of usage in ocean climate models. Shortly after being introduced, the GM90 scheme was shown to improve the representation of many flow features in global ocean circulation models, including the thermocline, water mass distribution, overturning circulation, and deep convection (Danabasoglu et al., 1994). Due to its great success, many modeling centers have adopted the GM90 parameterization (Gent, 2011), and the GM90 scheme is now employed in virtually every non-eddying ocean climate model (Griffies et al., 2016). In contrast, the GL90 scheme has seen only very limited use, and exclusively in models that (a) use z-coordinates and (b) are of coarse (>1°) grid spacing (Ferreira & Marshall, 2006; McWilliams & Gent, 1994; Saenz et al., 2015; Zhao & Vallis, 2008).

The objective of our study is to compare the GL90 and GM90 parameterizations in isopycnal coordinates, both from a theoretical and practical perspective, and across a range of non-eddying to eddy-permitting resolutions. To accomplish this goal, we work with a stacked shallow water model, which uses isopycnal coordinates in a fully adiabatic limit.

2. Averaged Stacked Shallow Water Equations

The stacked shallow water equations describe the equations of motion for layer thickness h_n, tracer concentration C_n, and horizontal velocity $\boldsymbol{u}_n = (u_n, v_n)$ in each layer $1 \le n \le N$ of constant density (Section 3.3 of Vallis (2017)):

$$\partial_t h_n + \nabla \cdot (h_n \boldsymbol{u}_n) = 0, \tag{2}$$

$$\partial_t C_n + \boldsymbol{u}_n \cdot \nabla C_n = 0, \tag{3}$$

$$\partial_t \boldsymbol{u}_n + \boldsymbol{u}_n \cdot \nabla \boldsymbol{u}_n + f \hat{\boldsymbol{z}} \times \boldsymbol{u}_n = -\nabla M_n + \boldsymbol{F}_n. \tag{4}$$

Here, ∇ denotes the two-dimensional horizontal gradient operator acting on fields within layers. In Equation 4, f is the Coriolis parameter,

$$M_n = \sum_{k=1}^{n} g^r_{k-1/2}\, \eta_{k-1/2} \tag{5}$$

is the shallow water Montgomery potential, and $\boldsymbol{F}_n$ describes the vertical stress divergence and horizontal friction terms. In the Montgomery potential, $g^{\mathrm{r}}_{k-1/2} = g(\rho_k - \rho_{k-1})/\rho_o$ and $\eta_{k-1/2} = -D + \sum_{i=k}^{N} h_i$ denote the reduced gravity and the interface height at interface $k - 1/2$, respectively, where ρ_o is the reference density, and D the ocean depth. Fields carrying a half-layer index, $k \pm 1/2$, live on layer interfaces.

The tracer Equation 3 and velocity Equation 4 are written in their advective form. Advective formulations lack conservative interpretations of both the eddy-mean field equations (as detailed in Appendix A) and numerical implementations. This limitation of the advective formulations is problematic since local and global conservation, especially for tracers, are essential for ocean circulation models used for climate studies (e.g., Griffies et al., 2016). We are thus motivated to consider the thickness-weighted equations, whereby advective transport appears as the divergence of a flux. The thickness-weighted equations offer an ideal framework for conservation, such as realized using finite volume methods (e.g., Griffies et al., 2020). For that purpose, we use the thickness Equation 2 to transform Equations 3 and 4 to thickness-weighted tracer and velocity equations

$$\partial_t(h_n C_n) + \nabla \cdot (h_n \boldsymbol{u}_n C_n) = 0, \tag{6}$$

$$\partial_t(h_n \boldsymbol{u}_n) + \nabla \cdot (h_n \boldsymbol{u}_n \otimes \boldsymbol{u}_n) + f\hat{\boldsymbol{z}} \times h_n \boldsymbol{u}_n = -h_n \nabla M_n + h_n \boldsymbol{F}_n. \tag{7}$$

2.1. Non-TWA Equations

Averaging the non-thickness-weighted Equations 2–4 leads to the following equation set:

$$\partial_t \overline{h}_n + \nabla \cdot \left(\overline{h}_n \overline{\boldsymbol{u}}_n + \overline{h'_n \boldsymbol{u}'_n} \right) = 0 \tag{8}$$

$$\partial_t \overline{C}_n + \overline{\boldsymbol{u}}_n \cdot \nabla \overline{C}_n + \overline{\boldsymbol{u}'_n \cdot \nabla C'_n} = 0 \tag{9}$$

$$\partial_t \overline{\boldsymbol{u}}_n + \overline{\boldsymbol{u}}_n \cdot \nabla \overline{\boldsymbol{u}}_n + \overline{\boldsymbol{u}'_n \cdot \nabla \boldsymbol{u}'_n} + f\hat{\boldsymbol{z}} \times \overline{\boldsymbol{u}}_n = -\nabla \overline{M}_n + \overline{\boldsymbol{F}}_n. \tag{10}$$

Here, $\overline{\cdot}$ denotes an along-isopycnal Reynolds average, and primed variables represent deviations from this average.

The eddy term in the averaged thickness Equation 8 can be related to the bolus velocity

$$\boldsymbol{u}^{\mathrm{bolus}}_n \equiv \frac{\overline{h'_n \boldsymbol{u}'_n}}{\overline{h}_n}, \tag{11}$$

arising from along-isopycnal correlations between thickness and horizontal velocity (Griffies, 2004; Rhines & Young, 1982). As anticipated at the start of this section, the eddy terms in the non-TWA tracer and velocity Equations 9 and 10 are not in the form of the divergence of a flux, and cannot be re-written in such a way. Instead, the eddy terms are non-conservative, which is associated with the fact that non-thickness-weighted averaging along isopycnal layers conserves neither tracers nor momentum (Appendix A).

2.2. TWA Equations

We now derive the TWA stacked shallow water equations. Our derivation can be viewed as a simpler (discrete) version of the analysis in Young (2012), who derived the TWA equations for continuous isopycnal coordinates. Following the notation in Young (2012), we define a TWA via

$$\widehat{C}_n = \frac{\overline{h_n C_n}}{\overline{h}_n}. \tag{12}$$

Deviations from this average are denoted by a double prime $''$. Since $\overline{\cdot}$ is a Reynolds average, so is the operator $\widehat{\cdot}$, though unlike $\overline{\cdot}$, the TWA $\widehat{\cdot}$ does not commute with derivatives.

We can derive the TWA equations by applying $\overline{\cdot}$ to the thickness Equation 2, as well as the thickness-weighted tracer and velocity Equations 6 and 7:

$$\partial_t \overline{h}_n + \nabla \cdot \left(\overline{h}_n \widehat{\boldsymbol{u}}_n \right) = 0, \tag{13}$$

$$\partial_t \left(\overline{h}_n \widehat{C}_n \right) + \nabla \cdot \left(\overline{h}_n \widehat{\boldsymbol{u}}_n \widehat{C}_n \right) = -\nabla \cdot \left(\overline{h}_n \widehat{\boldsymbol{u}_n'' C_n''} \right), \tag{14}$$

$$\partial_t \widehat{\boldsymbol{u}}_n + \widehat{\boldsymbol{u}}_n \cdot \nabla \widehat{\boldsymbol{u}}_n + \frac{1}{\overline{h}_n} \nabla \cdot \left[\overline{h}_n \widehat{\boldsymbol{u}_n'' \otimes \boldsymbol{u}_n''} \right] + f \hat{\boldsymbol{z}} \times \widehat{\boldsymbol{u}}_n = -\nabla \overline{M}_n - \widehat{\nabla M_n'} + \widehat{\boldsymbol{F}}_n. \tag{15}$$

In Equation 13, we have used the identity $\overline{h_n \boldsymbol{u}_n} = \overline{h}_n \widehat{\boldsymbol{u}}_n$. Equation 14 employs the identity $\overline{h_n \boldsymbol{u}_n C_n} = \overline{h}_n \widehat{\boldsymbol{u}_n C_n} = \overline{h}_n \left(\widehat{\boldsymbol{u}}_n \widehat{C}_n + \widehat{\boldsymbol{u}_n'' C_n''} \right)$, and Equation 15 the identity

$$\partial_t \widehat{\boldsymbol{u}}_n = \partial_t \left(\frac{\overline{h \boldsymbol{u}_n}}{\overline{h}_n} \right) = \frac{1}{\overline{h}_n} \partial_t \left(\overline{h \boldsymbol{u}_n} \right) - \frac{\widehat{\boldsymbol{u}}_n}{\overline{h}_n} \partial_t \overline{h}_n.$$

The TWA thickness Equation 13 contains no explicit eddy terms, but it is simply a re-writing of Equation 8 using different notation. The following identity relates the TWA, non-TWA, and bolus velocities:

$$\widehat{\boldsymbol{u}}_n = \overline{\boldsymbol{u}}_n + \frac{\overline{h_n' \boldsymbol{u}_n'}}{\overline{h}_n} = \overline{\boldsymbol{u}}_n + \widehat{\boldsymbol{u}_n'} = \overline{\boldsymbol{u}}_n + \boldsymbol{u}_n^{\text{bolus}}. \tag{16}$$

The TWA momentum Equation 15, in turn, contains not one, but two eddy terms: besides the nonlinear Reynolds stress term, we identify an eddy form stress term, which can also be written as

$$\overline{h}_n \widehat{\nabla M_n'} = \overline{h_n' \nabla M_n'}. \tag{17}$$

We note that, strictly speaking, $\overline{h}_n \widehat{\nabla M_n'}$ is the sum of the eddy form stress and a second term: an eddy pressure term (Appendix B). Greatbatch (1998) argues that this second term is negligibly small relative to the eddy form stress. We follow Greatbatch's assumption, and will hereafter refer to $\overline{h}_n \widehat{\nabla M_n'}$ simply as the "eddy form stress." To clarify the physical meaning of the eddy form stress, notice that $\nabla M_n = -f \hat{\boldsymbol{z}} \times \boldsymbol{u}_n^g$ where $\boldsymbol{u}_n^g$ is the geostrophic velocity, and thus

$$-\overline{h}_n \widehat{\nabla M_n'} = f \hat{\boldsymbol{z}} \times \overline{h_n' \boldsymbol{u}_n^{g\prime}} \approx f \hat{\boldsymbol{z}} \times \overline{h_n' \boldsymbol{u}_n'}, \tag{18}$$

where the approximate identity holds if $\boldsymbol{u}_n'$ is mostly geostrophic. The eddy form stress is therefore directly related to the geostrophic component of the eddy bolus velocity, $\overline{h_n' \boldsymbol{u}_n^{g\prime}} / \overline{h}_n$.

2.3. Consistency With Parameterizations

The purpose of this section is to connect the eddy terms in the respective equation sets Equations 8–10 and Equations 13–15 with commonly used eddy parameterizations in isopycnal coordinates. The discussion applies to isopycnal coordinate models like the Miami Isopycnic Coordinate Ocean Model (MICOM; Bleck et al., 1992) and the Bergen Layered Ocean Model (BLOM; Seland et al., 2020), to stacked shallow water models (Marques et al., 2022), and to the isopycnal coordinate regions of hybrid coordinate ocean models (e.g., Adcroft et al., 2019; Bleck, 2002; Ringler et al., 2013).

We first discuss the thickness equation. The bolus velocity (Equation 11) that appears in Equation 8 as part of the non-TWA framework is commonly parameterized by the GM90 eddy velocity (Gent et al., 1995). Therefore, the non-TWA thickness Equation 8 is consistent with model formulations that use the GM90 parameterization, if we interpret the GM90 eddy velocity as the bolus velocity.

We next consider the tracer equation. Isopycnal coordinate models often use two distinct parameterizations in the tracer equation: the GM90 eddy velocity (Gent et al., 1995) to advect tracers and volume, and along-isopycnal diffusion. The TWA tracer Equation 14 is in line with these conventions. Indeed, the TWA velocity in the advection term can be written as $\widehat{\boldsymbol{u}} = \overline{\boldsymbol{u}} + \boldsymbol{u}_n^{\text{bolus}}$ (Equation 16), where the bolus velocity is parameterized by GM90. The eddy term on the right hand side of Equation 14 can be parameterized in terms of a tracer mixing tensor (Griffies, 2004):

$$\widehat{\boldsymbol{u}_n'' C_n''} = -\mathbf{J} \cdot \nabla \widehat{C}_n. \tag{19}$$

Assuming that $\mathbf{J}$ is a positive-definite, symmetric, and isotropic tensor, it can be related to the small slope version of the isopycnal diffusion tensor (Gent & McWilliams, 1990). Note that the antisymmetric component of the along-isopycnal mixing tensor, which also acts as an eddy-induced advection, is not identified with the GM90 parameterization here. Whereas the TWA tracer equation is consistent with the usual treatment of along-isopycnal diffusion in isopycnal coordinate models, the non-TWA tracer Equation 9 is not. Specifically, the fact that the eddy term in the non-TWA tracer equation is non-conservative is contrary to how eddy terms are commonly parameterized in isopycnal coordinate models.

Finally, we turn to the momentum equation. The nonlinear Reynolds stress term in the TWA momentum Equation 15 conserves momentum, and corresponds naturally to commonly used viscous closures. However, the eddy term on the right hand side of the TWA momentum Equation 15, the eddy form stress (Equation 17), is currently not parameterized in isopycnal coordinate models (but could be parameterized by GL90, see Section 3). Considering the non-TWA momentum Equation 10, we make a similar observation as for the non-TWA tracer equation: the nonlinear eddy term is non-conservative, unlike commonly used viscous closures.

In summary, the GM90 parameterizations seen in, for example, MICOM and MOM6 are consistent with the non-TWA thickness equation and the TWA tracer equation, but neither the non-TWA nor the TWA momentum equation (see also McDougall & McIntosh, 2001). Note that all TWA Equations 13–15 are consistent with the stacked shallow water model equations, as long as no GM90 parameterization is used and the unresolved eddy form stress in the momentum equation is assumed negligible. This interpretation of the model equations is applicable for eddy-resolving simulations without GM90. For non-eddying simulations, GL90 provides an avenue to parameterize the eddy terms in a way that is fully consistent with the TWA framework, that is, equation set (Equations 13–15). This perspective motivates us to formulate and test a GL90 parameterization for the stacked shallow water equations in Sections 3 and 4.

3. The GM90 and GL90 Parameterizations in Isopycnal Coordinates

While previous studies have used the GL90 parameterization in z-coordinates (Appendix D), we now derive a GL90 vertical viscosity parameterization for the eddy form stress (Equation 17) in isopycnal coordinates. Using identity Equation 18, which relates the eddy form stress to the geostrophic component of the eddy bolus velocity, we can derive a formulation for the GL90 viscosity that makes the closure effectively equivalent to GM90 in the geostrophic limit.

In isopycnal coordinates, the eddy bolus transport is parameterized by GM90 as follows (e.g., Adcroft et al., 2019):

$$\sum_{i=1}^{N} \overline{h_i' \boldsymbol{u}_i'} = 0, \tag{20}$$

$$\sum_{i=n}^{N} \overline{h_i' \boldsymbol{u}_i'} = -\kappa_{n-1/2}^{\text{GM}} \nabla \bar{\eta}_{n-1/2}, \qquad 2 \le n \le N-1, \tag{21}$$

where the top layer is indexed by $n = 1$, and the bottom layer by $n = N$. The scalar $\kappa_{n-1/2} > 0$ is the interface height diffusivity associated with interface $n - 1/2$, and can vary in the horizontal and vertical. Identity Equation 20 enforces that the GM90 streamfunction is zero at the surface. Note that this is an assumption of the parameterization; in reality the left hand side of Equation 20 does not need to be zero.

For interior layers $1 < n < N$, the eddy form stress can now be written as

$$-\overline{h}_n\widehat{\nabla M'_n} = -\overline{h'_n\nabla M'_n} \approx f\hat{\boldsymbol{z}}\times\overline{h'_n\boldsymbol{u}'_n} \tag{22a}$$

$$= f\hat{\boldsymbol{z}}\times\left(\kappa^{\mathrm{GM}}_{n+1/2}\nabla\overline{\eta}_{n+1/2} - \kappa^{\mathrm{GM}}_{n-1/2}\nabla\overline{\eta}_{n-1/2}\right) \tag{22b}$$

$$= f\hat{\boldsymbol{z}}\times\left(\kappa^{\mathrm{GM}}_{n+1/2}\frac{\nabla\overline{\boldsymbol{M}}_{n+1}-\nabla\overline{\boldsymbol{M}}_n}{g^r_{n+1/2}} - \kappa^{\mathrm{GM}}_{n-1/2}\frac{\nabla\overline{\boldsymbol{M}}_n-\nabla\overline{\boldsymbol{M}}_{n-1}}{g^r_{n-1/2}}\right) \tag{22c}$$

$$\approx f^2\left(\kappa^{\mathrm{GM}}_{n-1/2}\frac{\hat{\boldsymbol{u}}_n-\hat{\boldsymbol{u}}_{n-1}}{g^r_{n-1/2}} - \kappa^{\mathrm{GM}}_{n+1/2}\frac{\hat{\boldsymbol{u}}_{n+1}-\hat{\boldsymbol{u}}_n}{g^r_{n+1/2}}\right). \tag{22d}$$

The two approximate identities above are based on an approximate geostrophic balance: the first applies to the eddies (see also Equation 18), and the second one is layer-wise geostrophic balance in the TWA momentum equation: $f\hat{\boldsymbol{z}}\times\hat{\boldsymbol{u}}_n \approx -\nabla\bar{M}_n$. The identities in Equations 22b and 22c use Equation 21 and the definition of the Montgomery potential (Equation 5), respectively. Approximate geostrophic balance (used twice), together with Equations 20 and 21, also implies that in the uppermost and lowermost layer, we have

$$-\overline{h}_1\widehat{\nabla M'_1} \approx f^2\left(-\kappa^{\mathrm{GM}}_{3/2}\frac{\hat{\boldsymbol{u}}_2-\hat{\boldsymbol{u}}_1}{g^r_{3/2}}\right), \tag{23}$$

$$-\overline{h}_N\widehat{\nabla M'_N} \approx f^2\left(\kappa^{\mathrm{GM}}_{N-1/2}\frac{\hat{\boldsymbol{u}}_N-\hat{\boldsymbol{u}}_{N-1}}{g^r_{N-1/2}}\right). \tag{24}$$

The expressions in Equations 22d, 23, and 24 contain only TWA quantities, and are the derived parameterization. This parameterization is a discretization of

$$-\widehat{\nabla M'} \approx \partial_z\left(\nu^{\mathrm{GL}}\,\partial_z\hat{\boldsymbol{u}}\right), \tag{25}$$

where the GL90 vertical viscosity at interface $n-1/2$ is given by

$$\nu^{\mathrm{GL}}_{n-1/2} = \kappa^{\mathrm{GM}}_{n-1/2}\left(f^2\frac{\bar{h}_{n-1}+\bar{h}_n}{2g^r_{n-1/2}}\right), \tag{26}$$

with stress-free boundary conditions at the top and bottom. Noting that the stratification in stacked shallow water is simply given by $N^2 = g'/h$, the expression in Equation 26 corresponds exactly to the vertical viscosity in Equation 1, as suggested in Greatbatch and Lamb (1990).

We implement the GL90 vertical viscosity scheme in MOM6's stacked shallow water configuration. Note that one achieves the correct top and bottom boundary conditions simply by setting the viscosities $\nu^{\mathrm{GL}}_{1/2}$ and $\nu^{\mathrm{GL}}_{N+1/2}$ to zero. The effect of these boundary conditions is similar to setting the GM90 streamfunction to zero at the boundaries. From a practical perspective, the implementation of GM90 can be delicate near in- and outcrops; MOM6's approach is to use limiters to avoid fluxing volume out of vanished layers. We find that special treatment for GL90 is not needed at the surface, but is indeed required near the bottom. To avoid spurious large bottom velocities over the continental slope, momentum needs to be prevented from being fluxed into vanished layers near the bottom, for example, through near-bottom tapering. Appendix C provides a detailed description of our GL90 implementation.

4. Simulations

In this section, we present idealized MOM6 simulations that use an isopycnal coordinate and either the GM90 or the GL90 parameterization. For GM90, we employ the scheme that was already implemented in MOM6; it acts via Equations 20 and 21 in the thickness equation. For GL90, we use our newly implemented scheme that applies the vertical viscosity (Equation 26) in the momentum equation. We then compare the effects of GM90 versus GL90 on the flow, including its energy levels, vertical structure, and energy transfers.

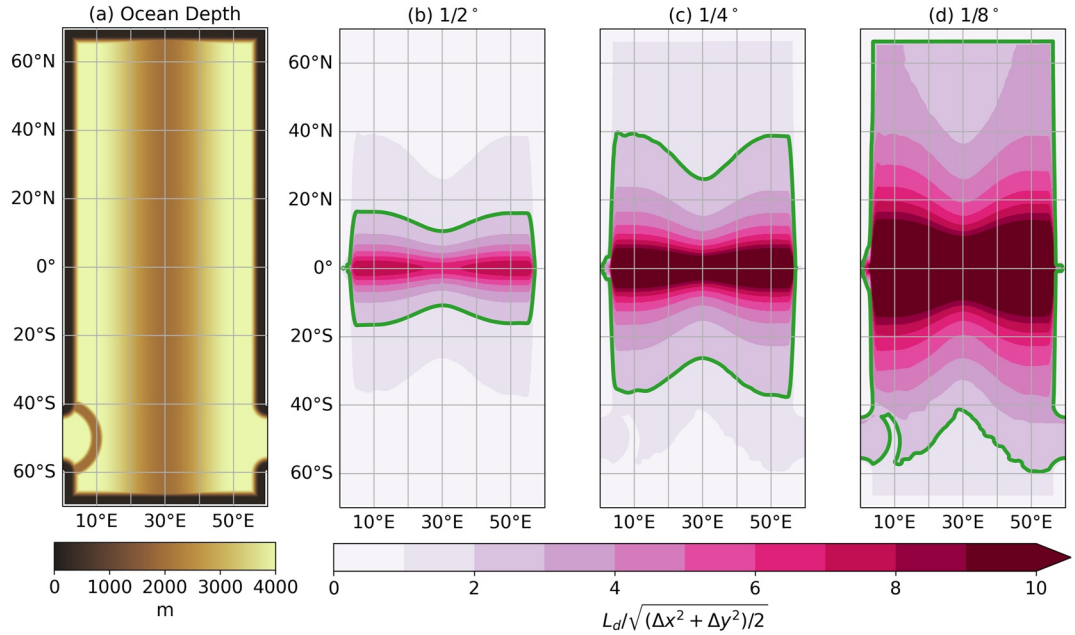

Figure 1. (a) Ocean depth in the NeverWorld2 configuration. (b–d) The ratio $L_d/\sqrt{(\Delta x^2+\Delta y^2)/2}$, where L_d is the first baroclinic Rossby radius, and Δx, Δy are the zonal and meridional grid spacings for horizontal grid spacings of (b) 1/2°, (c) 1/4°, and (d) 1/8°. The green contour line marks the case $L_d/\sqrt{(\Delta x^2+\Delta y^2)/2}=2$.

4.1. Model Configuration

We work within the NeverWorld2 configuration of MOM6 (Marques et al., 2022), which was specifically developed for the study of mesoscale eddy parameterizations. With a single cross-equatorial basin and a re-entrant channel in the Southern Hemisphere, the NeverWorld2 geometry means to represent idealized Atlantic and Southern Oceans (Figure 1a). Prominent features of the NeverWorld2 topography include an idealized Scotia Arc which partially blocks the re-entrant channel, an idealized mid-Atlantic ridge, and a continental shelf surrounding the Atlantic basin.

NeverWorld2 solves the stacked shallow water thickness and velocity Equations 2 and 4, with $N=15$ layers, on a regular spherical grid, and as discretized by the GFDL-MOM6 numerical ocean code (Adcroft et al., 2019). The NeverWorld2 setup does not include any tracers, so that in this section we focus on an analysis of circulation, flow, and energetics rather than tracer distributions. The term $\boldsymbol{F}_n$ in the velocity Equation 4 has a horizontal and vertical component. The horizontal component, $\boldsymbol{F}_n^h$, consists of a biharmonic Smagorinsky viscosity (Griffies & Hallberg, 2000). The vertical component contains the effects of wind forcing, bottom drag, and vertical viscosity,

$$\boldsymbol{F}_n^v=\boldsymbol{F}_n^{\text{wind}}+\boldsymbol{F}_n^{\text{drag}}+\boldsymbol{F}_n^{\text{visc}}. \tag{27}$$

Wind forcing is applied by a prescribed surface wind stress that is distributed over the top 20 m and is fixed in time and zonally constant (see Figure 1 in Marques et al. (2022)). The model uses a quadratic bottom drag law and a background kinematic vertical viscosity of 10^{-4} m^2 s^{-1}. The shallow water layers are immiscible, thus facilitating a relatively rapid spin-up of the configuration. More details on the NeverWorld2 model setup can be found in Marques et al. (2022).

4.2. Experiments

Marques et al. (2022) present NeverWorld2 simulations for grid spacings of 1/4°, 1/8°, 1/16°, and 1/32°, with these simulations using no mesoscale eddy parameterizations other than the biharmonic Smagorinsky viscosity and the background vertical viscosity; these simulations will hereafter be referred to as "unparameterized." In this study, we perform additional experiments at horizontal grid spacing of 1/2°, 1/4°, and 1/8° that use either the GM90 or the GL90 parameterization.

Table 1
Experiments Performed in This Study

	GM90	GL90
Grid spacing (°)	κ^{GM} (m^2 s^{-1})	ν^{GL} (m^2 s^{-1})
1/2	800	$800 \cdot f^2/N^2$
1/4	300	$300 \cdot f^2/N^2$
1/4	800	$800 \cdot f^2/N^2$
1/8	100	$100 \cdot f^2/N^2$
1/8	800	$800 \cdot f^2/N^2$

Note. Each row shows a pair of simulations that use either the GM90 or the GL90 parameterization; here, the value of ν^{GL} is inferred from the value of κ^{GM} under the assumption of quasi-geostrophy (see Equation 1). All GM diffusivities κ^{GM} are horizontally and vertically constant.

Figures 1b–1d show the diagnostic $L_d/\sqrt{(\Delta x^2+\Delta y^2)/2}$ for our three resolutions of interest, where

$$L_d = c_1/\sqrt{f^2+2\beta c_1} \tag{28}$$

is the first baroclinic deformation radius (Hallberg, 2013). Here, c_1 denotes the first-mode internal gravity wave speed, f the Coriolis parameter, and $\beta = \partial_y f$ its meridional gradient. Δx, Δy are the zonal and meridional grid spacings. A commonly used criterion for deeming mesoscale eddies resolved is $L_d/\sqrt{\left((\Delta x)^2+(\Delta y)^2\right)/2} \geq 2$, that is, at least two grid boxes need to fall within the deformation radius. Regions that are bounded by the green contour line are eddy-resolving according to this definition. Overall, Figures 1b–1d suggest that the grid spacings 1/2°, 1/4°, and 1/8° span a range from non-eddying to eddy-permitting dynamical regimes.

For each of the three grid spacings, we present multiple experiments that are summarized in Table 1 and Table S1 in Supporting Information S1. Each table row shows a pair of simulations that use either the GM90 or the GL90 parameterization. For each simulation pair, the ν^{GL} viscosity is inferred from the κ^{GM} diffusivity under the assumption of quasi-geostrophy (see Equation 1 and Section 3). Note that in the expressions for the ν^{GL} viscosities, the multiplier f^2/N^2 is shorthand for the term that appears in parentheses in Equation 26. Figure 2 highlights that, even if the κ^{GM} diffusivities are spatially constant (Table 1), the corresponding ν^{GL} viscosities are spatially varying - both in the vertical (set by $1/N^2$) and the horizontal (set by $1/N^2$ and f^2). In the following, we will refer to the experiments in the first row of Table 1 as "1/2° GM 800" and "1/2° GL 800," and similarly for the experiments in the other rows.

We focus on the experiments shown in Table 1, in which the GM diffusivity, κ^{GM}, is horizontally and vertically constant. While some ocean models still employ a spatially constant κ^{GM}, the modeling community has mainly moved toward using a spatially varying κ^{GM} coefficient that sometimes has smaller values in eddy-permitting than in non-eddying parts of the domain. For the purpose of simplicity, we nevertheless present our comparison of GM90 versus GL90 for spatially constant κ^{GM} (and corresponding $\nu^{GL} = \kappa^{GM} f^2/N^2$). In the Supporting Information S1 we present additional experiment pairs where we vary κ^{GM} spatially according to modern modeling approaches (Table S1 in Supporting Information S1). The main conclusions of this paper are the same, no matter if we draw them from the experiments in Table 1 or Table S1 of Supporting Information S1; in other words, our conclusions do not depend on the chosen spatial structure of κ^{GM}.

With finer grid spacing, eddies are increasingly resolved, and the GM90 or GL90 parameterizations are needed less. Therefore, we choose gradually decreasing κ^{GM} diffusivities of 800, 300, and 100 m^{2}s^{-1}, as the model's horizontal grid is refined from 1/2° to 1/8°. These κ^{GM} values, and corresponding ν^{GL} values, are tuned so that for each grid spacing, the GL90 work matches offline energy transfer diagnostics, see Section 4.5. In addition, we present experiment pairs at 1/4° and 1/8° grid spacing in which κ^{GM} is not reduced, but is kept at 800 m^{2}s^{-1}. We note that an unmodified, rather large, κ^{GM} would be an undesirable choice in eddy-permitting model simulations that aim at maximum realism because a strongly enabled GM90 or GL90 parameterization would excessively damp existing eddies. Even so, since the purpose of our study is to compare GM90 and GL90, we augment our list of test cases with simulations that have grid spacing 1/4° and finer *and* strongly active parameterizations.

The 1/2° simulations are initialized from rest, and run for 77,000 days to a quasi-steady state in which KE and APE are no longer drifting (Figures 3a and 3b). The 1/4° and 1/8° simulations are a continuation of the 1/4° and 1/8° simulations presented in Marques et al. (2022) (black lines in Figures 3c–3f); that is, we initialize our simulations with the states that Marques et al. (2022) obtained at their final time stamp. The 1/4° simulations are run for a total of 77,000 days, and the 1/8° simulations for a total of 28,000 days. Whenever we report time-averaged diagnostics in the following, the diagnostics are averaged over the last 2,000 days of the respective simulation (gray shading, Figure 3).

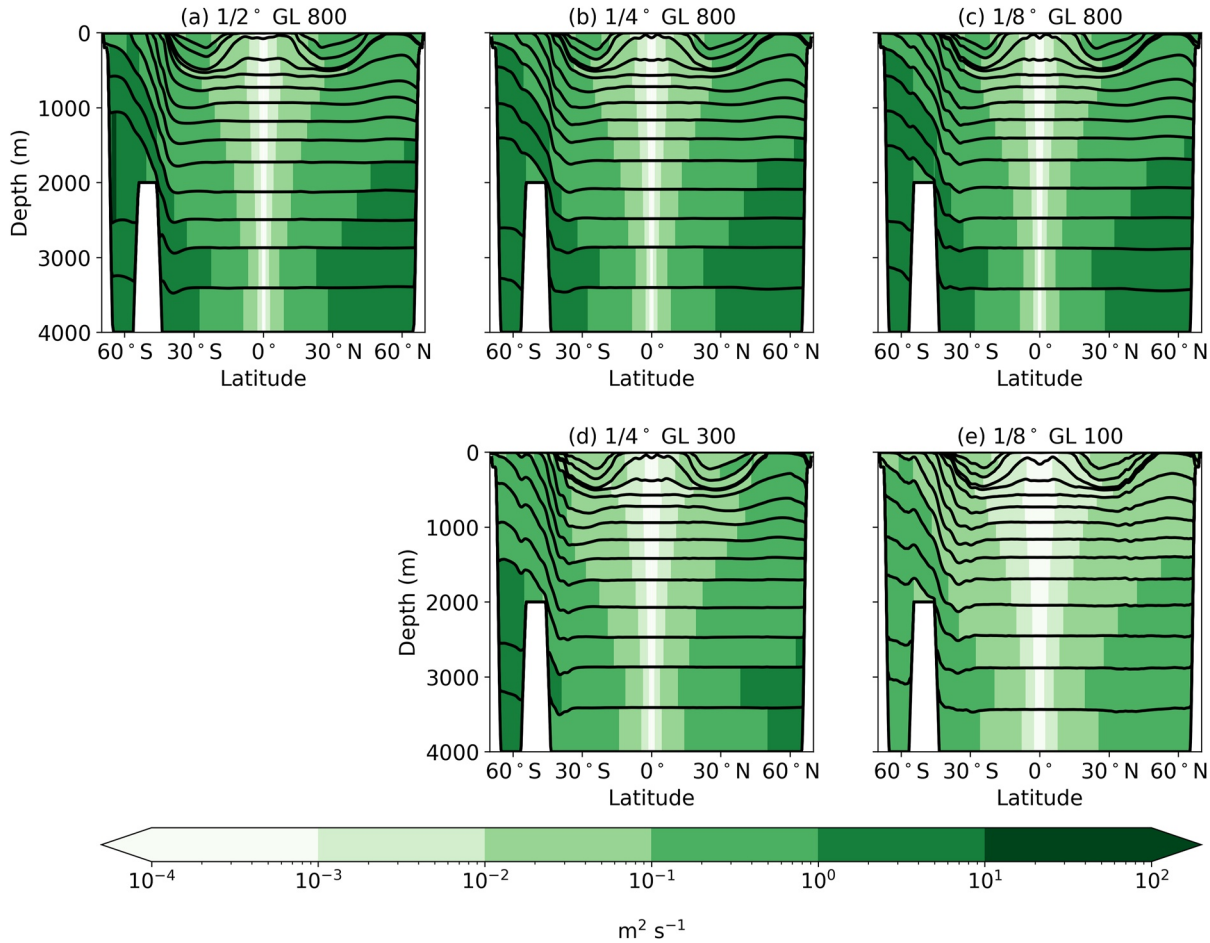

Figure 2. 2,000-day averaged GL90 vertical viscosity ν^{GL} (green shading) and layer interfaces (black lines) along a south-north transect at 10°E for the five GL90 experiments in Table 1. Note that the background vertical viscosity is 10^{-4} m^2 s^{-1}, that is, orders of magnitude smaller than the GL90 vertical viscosity except in the equatorial region.

4.3. Effects on Energy

We first examine the effects of the GM90 and GL90 parameterizations on energy. The depth-integrated KE and APE are given by

$$\mathrm{KE} = \frac{1}{2}\sum_{n=1}^{N} h_n\left(u_n^2 + v_n^2\right), \tag{29}$$

$$\mathrm{APE} = \frac{1}{2}\sum_{n=1}^{N} g^r_{n-1/2}\left(\eta^2_{n-1/2} - \max\left(z^0_{n-1/2}, -D\right)^2\right), \tag{30}$$

where $z^0_{n-1/2}$ is a constant nominal position for each interface. In other words, the APE in Equation 30 is defined as the depth-integrated PE minus the depth-integrated PE of the resting state. Each GM90 and GL90 simulation pair reaches very similar KE and APE levels (Figure 3). Upon averaging over the last 2,000 days of each simulation, the energy levels in the respective GM90 and GL90 pairs differ by less than 5% in all cases.

For the 1/4° and 1/8° experiments, we can compare the effect of different magnitudes of κ^{GM} and ν^{GL}. The simulations with $\kappa^{GM} = 800$ m^{2}s^{-1} and $\nu^{GL} = 800 \cdot f^2/N^2$ m^{2}s^{-1} lead to lower energy levels than the simulations with smaller κ^{GM} and ν^{GL} (Figures 3c–3f). This energy drop is expected as GM90 drains the wind-generated APE, where wind is the only external source of KE in these adiabatic simulations. Figure 3 suggests that GL90 has the exact same effect, as is expected under the assumption of quasi-geostrophy.

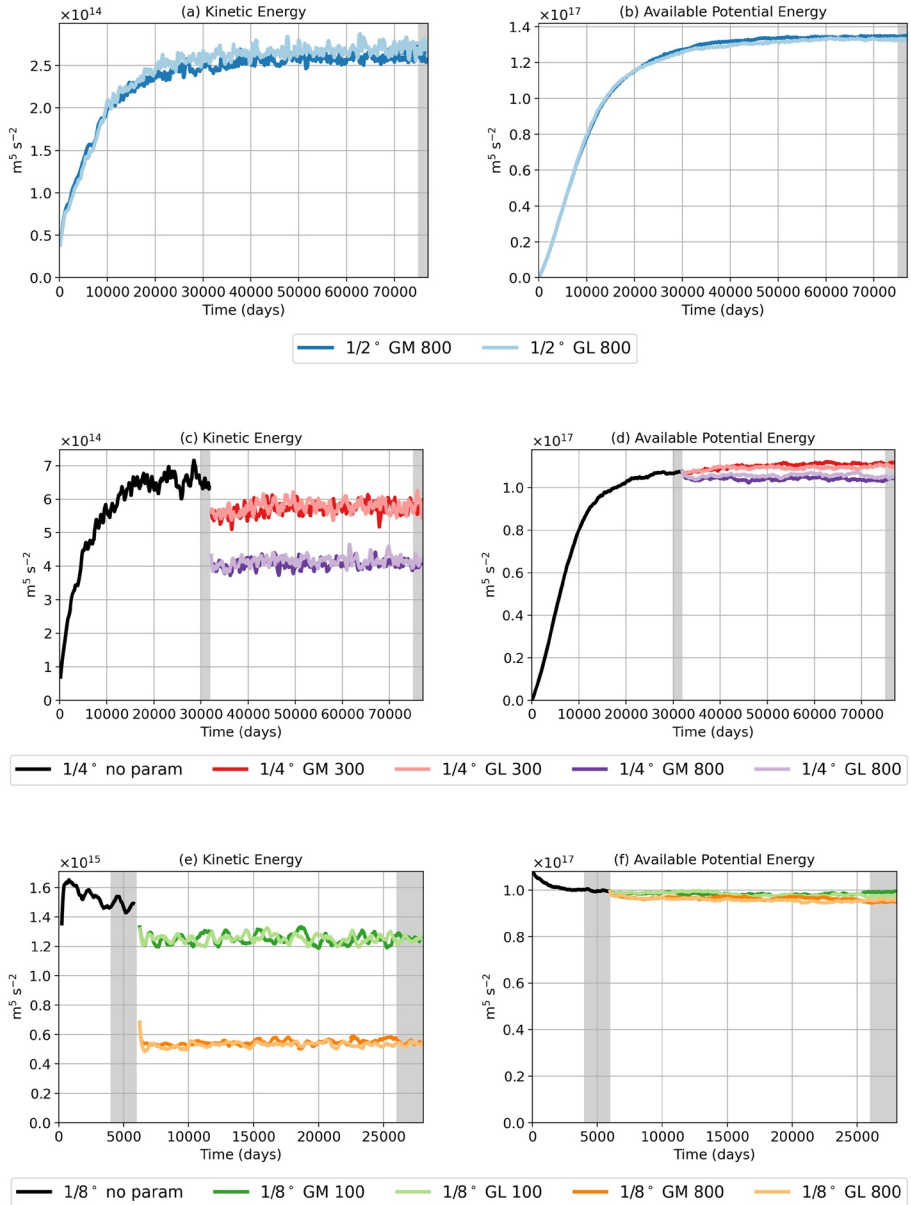

Figure 3. Timeseries of domain-integrated (a, c, and e) kinetic energy (Equation 29) and (b, d, and f) available potential energy (Equation 30) for the (a and b) 1/2°, (c and d) 1/4°, and (e and f) 1/8° simulations in Table 1, during spin-up and equilibration. The black lines depict the energy levels of the unparameterized 1/4° (in (c and d)) and 1/8° (in (e and f)) NeverWorld2 simulations presented in Marques et al. (2022). For the sake of clarity, (a, c, and e) show 100-day rolling averages that smooth out high-frequency variability. The gray shading marks the 2,000-day windows that are used for time-averaged diagnostics in other figures.

Next, we compute zonal spectra of surface eddy KE (Figure 4). We consider three latitude bands: 35–45°N, containing the Gulf Stream-like flow; 10–20°N, containing the energetic subtropical return flows; and 45–55°S, containing the ACC-like channel flow. The GM90 and GL90 simulation pairs show very similar energy spectra, with one exception: In the Gulf Stream region, the GL 800 experiments show lower surface KE than the corresponding GM 800 experiments, at all horizontal resolutions (Figures 4a, 4d, and 4g). This difference in the Gulf Stream region will be further examined in the next subsection.

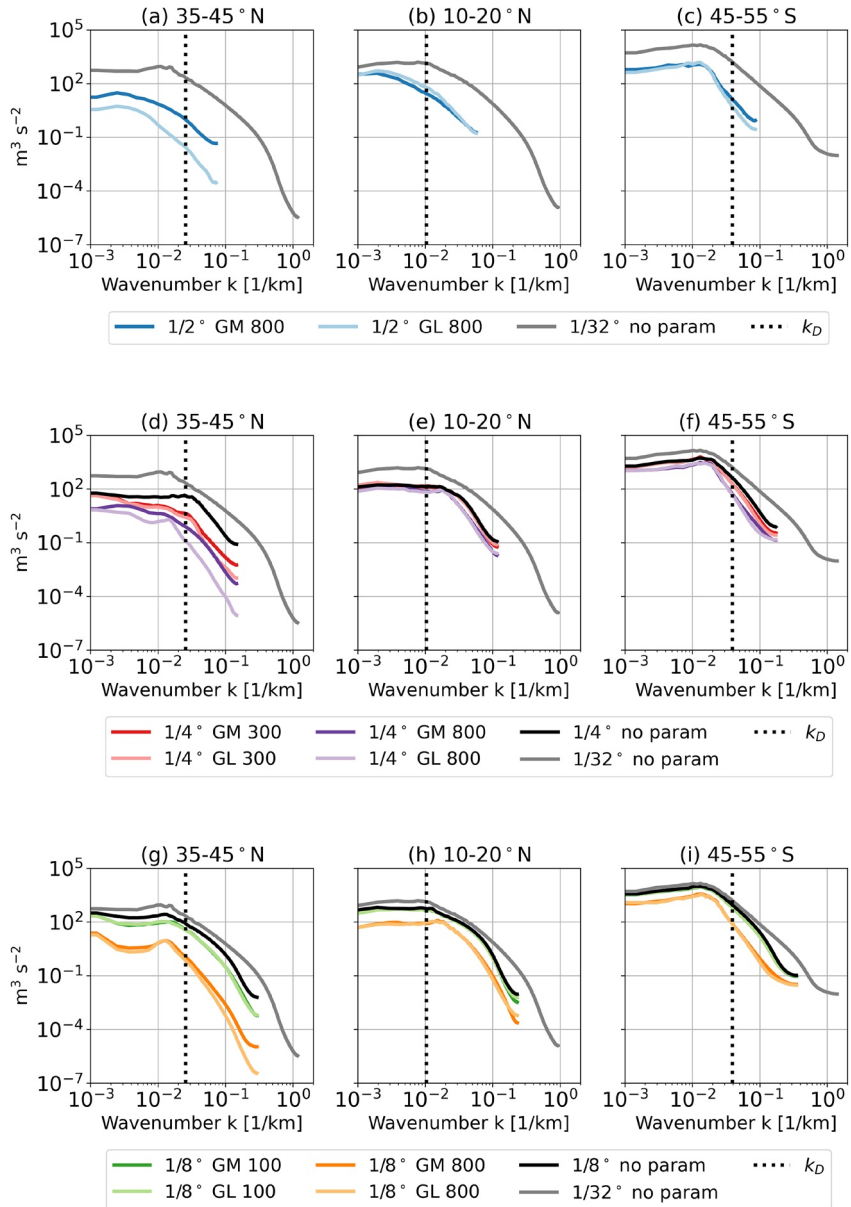

Figure 4. Zonal spectra of surface eddy kinetic energy for the (a–c) 1/2°, (d–f) 1/4°, and (g–i) 1/8° simulations from Table 1, and for three latitude bands (left to right): 35–45°N, 10–20°N, and 45–55°S. The spectra are computed from surface eddy velocities u' and v', defined as deviations from the 2,000-day averaged velocities. Within each latitude band, the one-dimensional zonal spectrum is computed at each latitude: $\left(|\mathcal{F}_x(u')|^2 + |\mathcal{F}_x(v')|^2\right)/2$, where $\mathcal{F}_x$ denotes Fourier transform in the x-direction, and then averaged across the latitude band and 2,000 days. For the bands of 35–45°N and 10–20°N, a Hann smoothing window is applied to make u' and v' periodic in the x-direction. Linear detrending is used in all cases. The black and gray lines show spectra from unparameterized NeverWorld2 simulations described in Marques et al. (2022). The dotted black line marks the wavenumber k_D corresponding to the first baroclinic deformation radius.

4.4. Effects on Flow Vertical Structure

The Gulf Stream is the only region in which we noted significant differences between the GM90 and GL90 simulations in Section 4.3. Figure 5 investigates this region further; it shows snapshots of the zonal flow in the northwestern Atlantic, along a south-north transect at 7°E. This transect contains the separated Gulf Stream. We first focus on the 1/2° simulations. At first glance, the GM90 simulation (Figure 5a) appears to have deeper reaching (albeit weak) jets than the GL90 simulation (Figure 5b), indicative of a more barotropic flow.

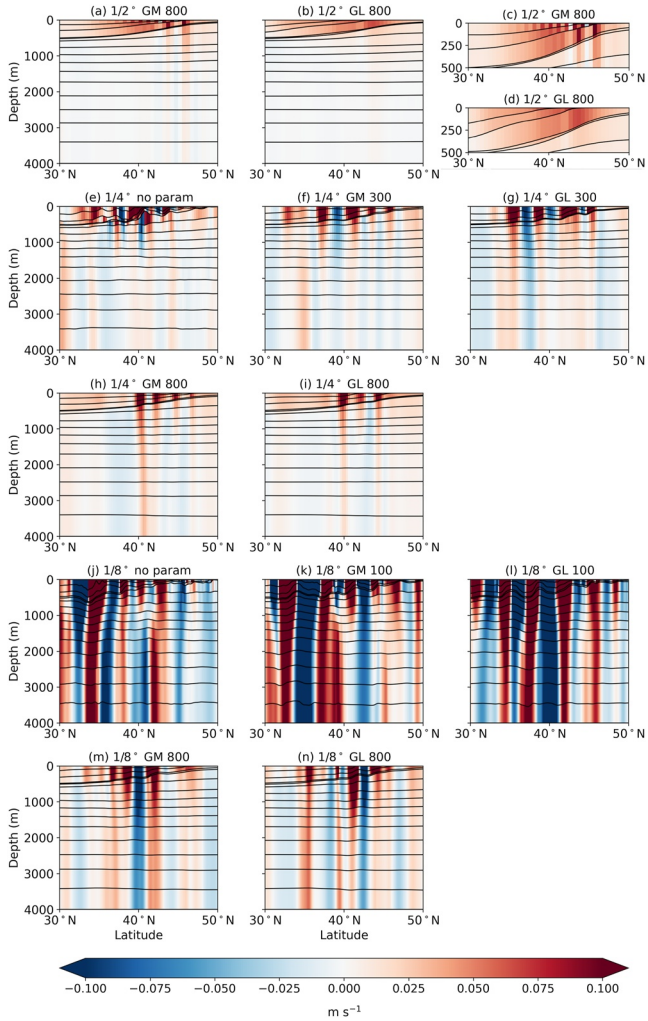

Figure 5. Snapshots of zonal velocity (shading) and layer interfaces (black lines) along a south-north transect at 7°E for all experiments in Table 1. Panels (c and d) are identical to (a and b), but zoomed into the upper 500 m. The snapshots in (e) and (j) are from the unparameterized NeverWorld2 simulations presented in Marques et al. (2022).

The next figure will investigate the barotropic fraction of the flow more systematically, that is, for the full domain and beyond a single snapshot.

A second notable feature in the 1/2° simulations is the difference in the surface flow. The surface velocity in the GM90 simulation has a checkerboard pattern (Figure 5c), while the surface flow in the GL90 simulation is much smoother (Figure 5d). We suggest that the noisy surface velocities in the GM90 simulation are a numerical artifact of how the GM90 parameterization treats in- and outcropping layers: limiters are required to avoid fluxing volume out of vanished layers. In contrast, the GL90 parameterization does not require extra or ad-hoc treatment near the surface, and leads to a more realistic surface flow distribution (at least in the horizontal). The noisy surface velocities seen in the 1/2° GM90 simulation also explain why the GM90 simulation has a surface KE spectrum that is elevated compared to that of the GL90 simulation (Figure 4a). In summary, the higher KE values that we noticed for the 1/2° GM90 simulation in the Gulf Stream region (Section 4.3) are due to numerical artifacts.

The 1/4° simulations (Figures 5e–5i) are characterized by a stronger and more barotropic flow than the 1/2° simulations. Intensity and barotropic fraction of the flow are further increased in the 1/8° simulations (Figures 5j–5n). This increase is expected since more vigorous eddy activity energizes and barotropizes the flow. For the 1/4° and 1/8° experiments, the GM90 and GL90 simulation pairs do not reveal systematic differences in their flow structure. It is worth noting that the 1/4° and 1/8° GM 800 simulations show a somewhat noisy surface flow further east in the North Atlantic (not shown), similar to that seen for the 1/2° GM90 simulation. Again, the noisy surface velocities for the GM 800 simulations explain the fact that the surface KE spectra are raised compared to those of the GL 800 simulations (Figures 4a, 4d, and 4g).

To further assess the effect of the GM90 and GL90 parameterizations on the flow vertical structure, we follow Yankovsky et al. (2022) and consider the fraction between the barotropic (BT) and total KE:

$$\frac{\mathrm{KE_{BT}}}{\mathrm{KE}} = \frac{\left(\sum_{n=1}^{N} h_n\right)\left(u_{\mathrm{BT}}^2 + v_{\mathrm{BT}}^2\right)}{\sum_{n=1}^{N} h_n\left(u_n^2 + v_n^2\right)}, \tag{31}$$

where the barotropic velocity is computed as

$$\boldsymbol{u}_{\mathrm{BT}} = \frac{\sum_{n=1}^{N} h_n \boldsymbol{u}_n}{\sum_{n=1}^{N} h_n}. \tag{32}$$

If the BT KE fraction (Equation 31) is equal to 1, the KE is fully contained in the barotropic mode, while a value of 0 indicates that the KE is fully contained in the baroclinic modes.

Figure 6 shows the zonally and 2,000-day averaged BT KE fraction for all experiments in Table 1. With finer resolution, the flow becomes increasingly barotropic because more resolved eddies and baroclinic instability barotropize the flow (Kjellsson & Zanna, 2017; Salmon, 1980; Scott & Wang, 2005; K. S. Smith & Vallis, 2001). The two experiments in each GM90 and GL90 simulation pair show an almost identical vertical structure (Figures 6a–6e), with one minor exception: for a horizontal grid spacing of 1/2°, the GM90 and GL90 simulations show differences in their BT KE fraction within the 25°S–25°N latitude band. This discrepancy may be associated with the breakdown of the geostrophic assumption at low latitudes. For horizontal grids of 1/4° and 1/8°, however, GM90 and GL90 do not lead to significantly different vertical structures near the equator (Figures 6b–6e).

Finally, we note that the 1/4° GM90 and GL90 simulations have a more barotropic flow than the unparameterized 1/4° simulations (Figures 6b and 6c). This result is anticipated because the GL90 parameterization explicitly mixes momentum downward, thus pushing KE into the barotropic mode. Figure 6 suggests that the GM90 parameter-

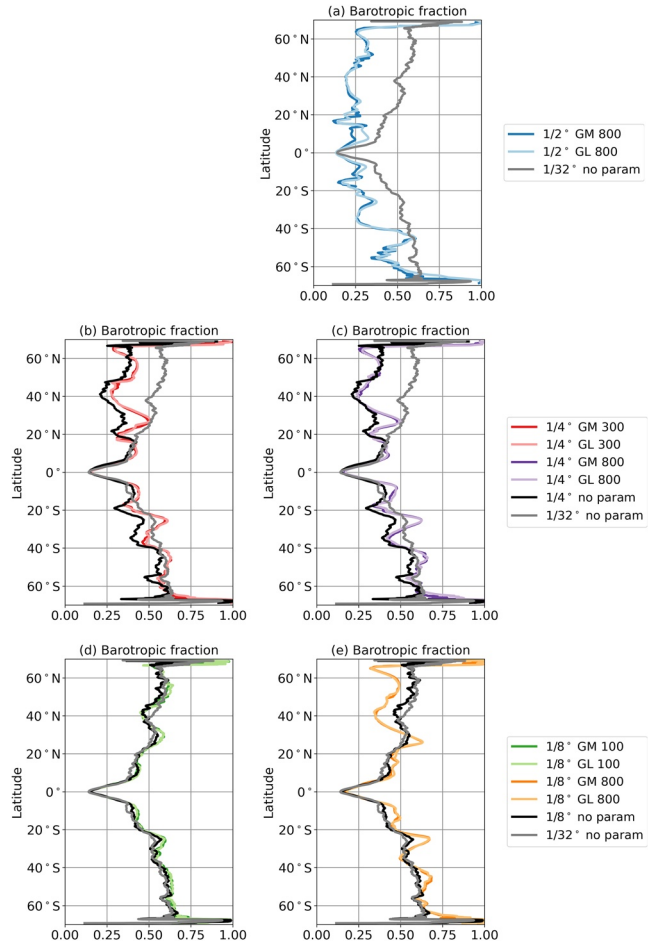

Figure 6. Zonally and 2,000-day averaged ratio of the barotropic kinetic energy (KE) to the total KE (Equation 31) for all experiments in Table 1. The black and gray lines depict ratios from the unparameterized NeverWorld2 simulations presented in Marques et al. (2022).

ization has the exact same effect, as is expected under the assumption of quasi-geostrophy. At a horizontal grid spacing of 1/8°, GM90 and GL90 do not lead to a significant barotropization compared to the unparameterized 1/8° simulation (Figures 6d and 6e). Figure 6e also exemplifies that choosing high κ^{GM} and ν^{GL} values at eddy-permitting resolution can make the flow more *baroclinic* rather than more barotropic (here: north of 30°N), possibly because exaggerated κ^{GM} and ν^{GL} coefficients damp existing eddies that would otherwise barotropize the flow.

4.5. Effects on Energy Budgets

In this section, we investigate the effects of the GM90 and GL90 parameterizations on the KE and PE budgets. The dynamic component of depth-integrated PE excludes the bottom contribution and is given by

$$\mathrm{PE} = \frac{1}{2}\sum_{n=1}^{N} g'_{n-1/2}\eta^2_{n-1/2}. \tag{33}$$

The budgets for the KE and PE reservoirs are

$$\begin{aligned}\partial_t(\mathrm{KE}) = &-\sum_{n=1}^{N}\nabla\cdot(\boldsymbol{u}_n\mathrm{KE}_n) - \sum_{n=1}^{N} h_n\boldsymbol{u}_n\cdot\nabla M_n + \sum_{n=1}^{N} h_n\boldsymbol{u}_n\cdot\boldsymbol{F}^{\mathrm{wind}}_n \\ &+\sum_{n=1}^{N} h_n\boldsymbol{u}_n\cdot\boldsymbol{F}^{\mathrm{drag}}_n + \sum_{n=1}^{N} h_n\boldsymbol{u}_n\cdot\boldsymbol{F}^{\mathrm{visc}}_n + \sum_{n=1}^{N} h_n\boldsymbol{u}_n\cdot\boldsymbol{F}^{h}_n + \mathrm{GL\,work},\end{aligned} \tag{34}$$

$$\partial_t(\mathrm{PE}) = -\sum_{n=1}^{N} \nabla \cdot \left(h_n \left(\boldsymbol{u}_n + \boldsymbol{u}_n^{\mathrm{GM}}\right) M_n\right) + \sum_{n=1}^{N} h_n \boldsymbol{u}_n \cdot \nabla M_n + \text{ GM work}, \tag{35}$$

where $\boldsymbol{u}_n^{\mathrm{GM}}$ is the GM90 bolus velocity and the energetics associated with the GM90 and GL90 parameterizations are the negative-definite terms

$$\text{GM work } = -\sum_{n=0}^{N-1} \kappa_{n+1/2}^{\mathrm{GM}}\, g_{n+1/2}^{r} |\nabla \eta_{n+1/2}|^2, \tag{36}$$

$$\text{GL work } = -f^2 \sum_{n=1}^{N-1} \frac{\kappa_{n+1/2}^{\mathrm{GM}}}{g_{n+1/2}^{r}} (\boldsymbol{u}_n - \boldsymbol{u}_{n+1})^2, \tag{37}$$

see Marques et al. (2022) and Loose et al. (2022) for a derivation.

Note that the first term on the right hand side of Equations 34 and 35 is an advection term, which integrates to zero over the domain (and will therefore not be considered in the following). The second term on the right hand side of Equation 34 is identical to the second term on the right hand side of Equation 35, but of opposite sign; this term describes conversion between KE and PE. The remaining terms on the right hand side of Equation 34 are the wind work, dissipation by bottom drag, dissipation by the background vertical viscosity, and dissipation by horizontal viscosity.

The first two columns of Figure 7 show the domain-integrated and 2,000-day averaged KE budgets, diagnosed online for six experiments from Table 1. From left to right, the terms are in the same order as they appear in Equation 34. For reference, we also show the work done by the GM90 parameterization (gray with dots), even though this term is part of the PE budget (Equation 35) rather than the KE budget. Note that the KE tendency term (on the left hand side of Equation 34) is negligible over long time averages, and the budgets shown in Figure 7 therefore close.

We can now compare the KE budget for each GM90 and GL90 simulation pair. Wind work (green bars) acts as a large KE source with comparable magnitudes across the GM90 and GL90 experiments in each simulation pair. In the GM90 simulations, the majority of this KE gets converted to PE (red bars), from where it gets extracted by the GM90 parameterization (gray bars with dots). In contrast, the GL90 simulations show no conversion to PE (in the domain integral). Instead, GL90 extracts a comparable amount of energy directly from the KE reservoir through dissipation via the GL90 vertical viscosity (pink bars). Bottom drag, background vertical viscosity and horizontal viscosity all act as KE sinks, and each of these sinks has comparable magnitudes across the GM90 and GL90 experiments in each simulation pair (with slightly more negative values in the GM90 simulations).

The third column of Figure 7 shows the "true" KE budget, diagnosed from the 1/32° NeverWorld2 simulation via an offline filtering approach (Loose et al., 2022). Here, we assume that the filter scale reflects the *effective* grid spacing of a model and that the model's effective spacing is four times larger than the model's grid scale (Kent et al., 2014; Loose et al., 2022; Skamarock, 2004; Soufflet et al., 2016). In short, the bars in Figures 7c, 7f, and 7i (corresponding to model grid scales of 1/2°, 1/4°, and 1/8°) reflect the mean kinetic energy (MKE) budgets from Figures 8b–8d in Loose et al. (2022) (corresponding to filter scales of 2°, 1°, and 1/2°). The offline KE budget (third column) is diagnosed within a TWA framework and can therefore only be compared to the online KE budget of the GL90 simulations (second column). The pink hatched bar is the diagnosed MKE extraction (and eddy KE production) through eddy form stress in the TWA framework, so should be compared to the GL90 work in the parameterized simulations in this work. For each horizontal resolution, the online GL90 work (pink bar) and its offline diagnosed counterpart (pink hatched bar) agree to within 4%. In fact, the values of κ^{GM} and corresponding ν^{GL} in Table 1 were tuned with the goal to achieve this match.

The offline diagnosed nonlinear KE exchange term (blue hatched bar) is due to eddy momentum fluxes, and can be seen as the sum of two terms: a (here dominating) positive-definite term, which reflects gain of large-scale KE through an inverse cascade, and a negative-definite term, which reflects extraction of large-scale KE by barotropic instability. In the simulations in this work, the nonlinear KE exchange term is to be parameterized. One could argue that the positive-definite contribution (representing the effect of a KE inverse cascade) can be parameterized through backscatter (e.g., Bachman, 2019; Jansen & Held, 2014; Jansen et al., 2019; Juricke et al., 2020;

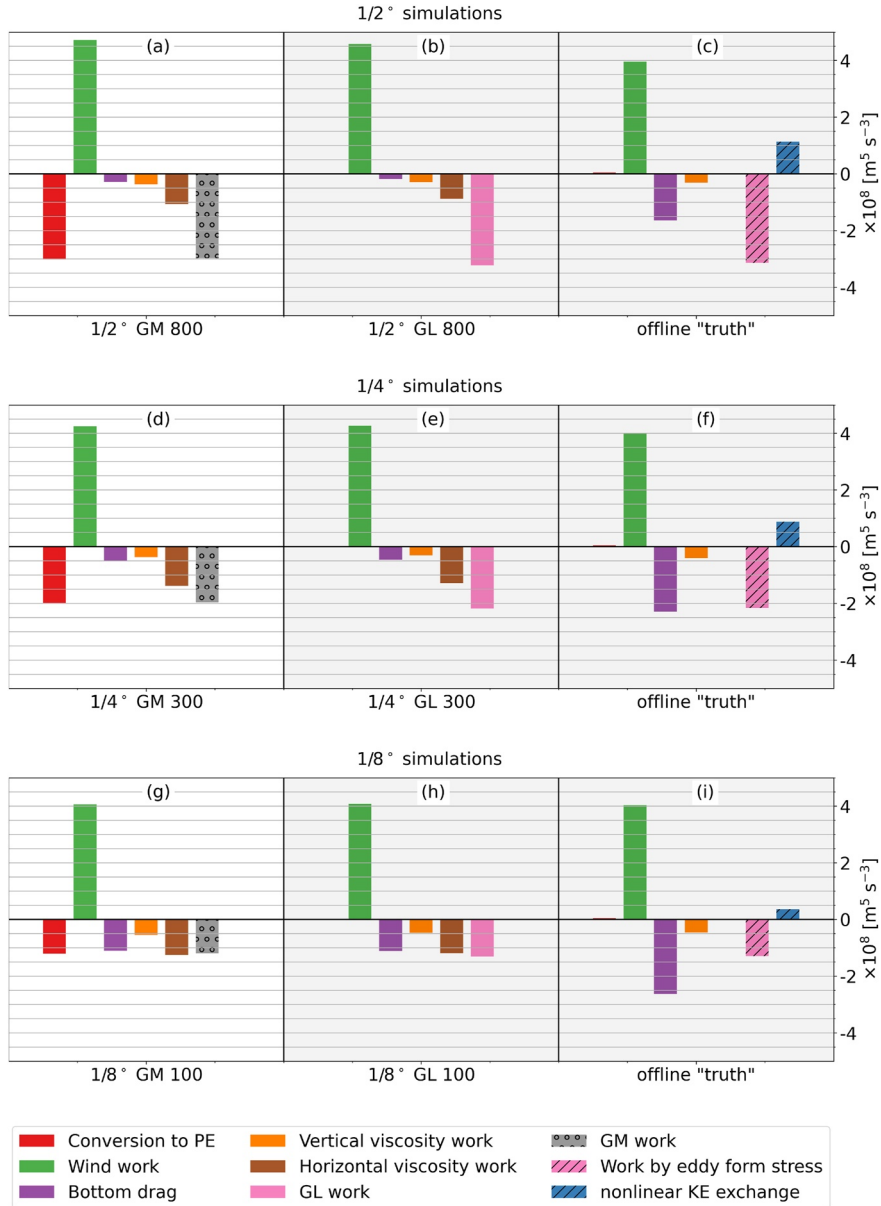

Figure 7. Domain-integrated and 2,000-day averaged kinetic energy (KE) budget (Equation 34) for the GM90 simulations (first column) and GL90 simulations (second column) in the (a and b) 1/2°, (d and e) 1/4°, and (g and h) 1/8° simulation from Table 1. For reference, the third column shows the "true" KE budget, diagnosed from the 1/32° NeverWorld2 simulation via an offline spatial filtering approach (Loose et al., 2022). The offline budget (third column) is diagnosed for a thickness-weighted averaged framework, and can therefore only be compared to the GL90 simulations (second column). In the first column, we also show the GM work term even though it is part of the potential energy budget (Equation 35) rather than the KE budget.

Zanna et al., 2017), and the negative-definite term (representing barotropic instability) can be parameterized by horizontal viscosity. Our simulations only use a horizontal viscosity but no backscatter parameterization. Subtracting the horizontal viscosity work (brown bars) in the second column from the nonlinear KE exchange term (blue hatched bars) in the third column makes clear that our simulations would benefit from a backscatter parameterization. For each horizontal resolution, the missing backscatter parameterization would require to add a similar amount of KE as is extracted by GL90. This result suggests that although the 1/2° degree simulations here are non-eddying, backscatter would still be energetically appropriate.

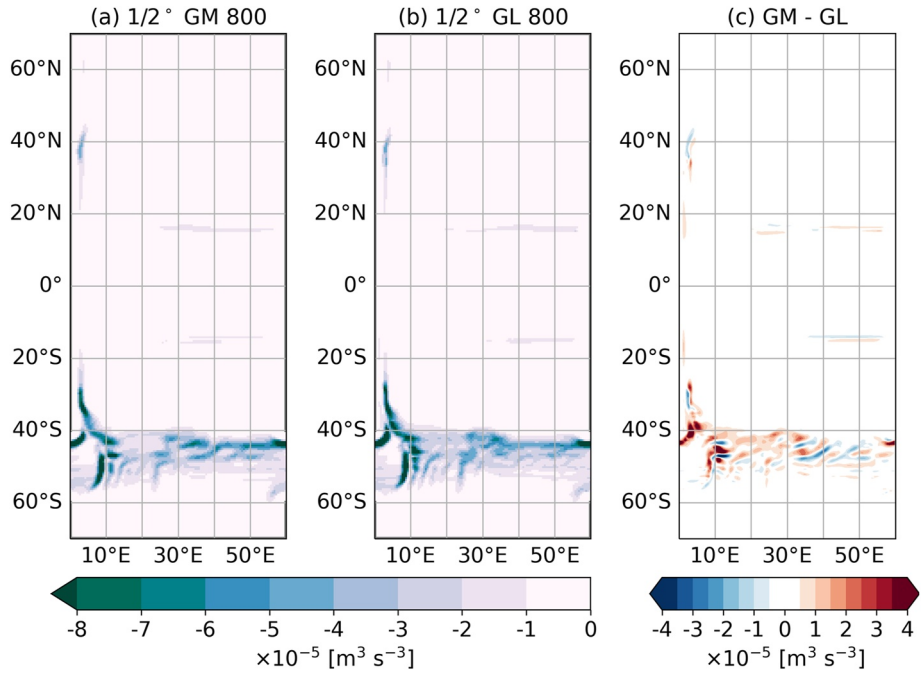

Figure 8. Energetics of the GM90 and GL90 parameterizations, diagnosed online from the 1/2° simulations in Table 1: (a) GM work (Equation 36) and (b) GL work (Equation 37), both depth-integrated and averaged over 2,000 days. (c) Difference of the GM and GL work terms, computed by subtracting (b) from (a). Red (blue) shading indicates that the GL (GM) work is of greater absolute value.

Finally, we note that the parameterized simulations in this work dissipate too little energy via bottom drag (purple bars). This shortcoming is caused by too weak bottom velocities in our parameterized simulations, which in turn could be due to two reasons: (a) a flow that is generally too weak, that is, not energetic enough; (b) a flow that is not barotropic enough so that bottom velocities stay weak. We suggest that (a) is the main player because the 1/8° GL 100 simulation has the same barotropic KE fraction as the 1/32° "truth" simulation (Figure 6d) but nevertheless dissipates less than half the KE via bottom drag compared to the 1/32° simulation. We suggest that adding a backscatter parameterization to our simulations would remedy (a), and ameliorate the problem of too little bottom drag dissipation. This hypothesis should be tested in future work.

Before concluding this section, we compare the GM work and the GL work more closely for our 1/2° simulations. We re-emphasize that the GM work acts as a sink for the PE reservoir (Equation 35), while the GL work acts as a sink for the KE reservoir (Equation 34). However, despite their inherently different energetic pathways, the horizontal distributions of the depth-integrated GM versus GL work show a very similar large-scale structure (Figures 8a and 8b). Upon inspecting their difference, we find that the GM and GL work differ on smaller scales, where the GL work tends to be of slightly greater magnitude (Figure 8c).

4.6. Computational Performance

We are interested in comparing the GM90 and GL90 parameterizations in terms of their computational needs. To this aim, we analyze the runtime for three GM90 and GL90 simulation pairs from Table 1, one for each horizontal grid (Figure 9). For each GM90 and GL90 simulation pair, the runtimes are normalized by the total runtime of the respective GM90 simulation. For the analysis in Figure 9, each experiment was run for 1,000 experiment days on NCAR's Cheyenne supercomputer (Computational And Information Systems Laboratory, 2017), on two nodes (for the 1/2° experiments) and eight nodes (for the 1/4° and 1/8° experiments) with 36 CPUs per node. There is no reason to expect significantly different *relative* runtimes across the three resolutions; we consider the runtime values merely as three samples from a (small) ensemble.

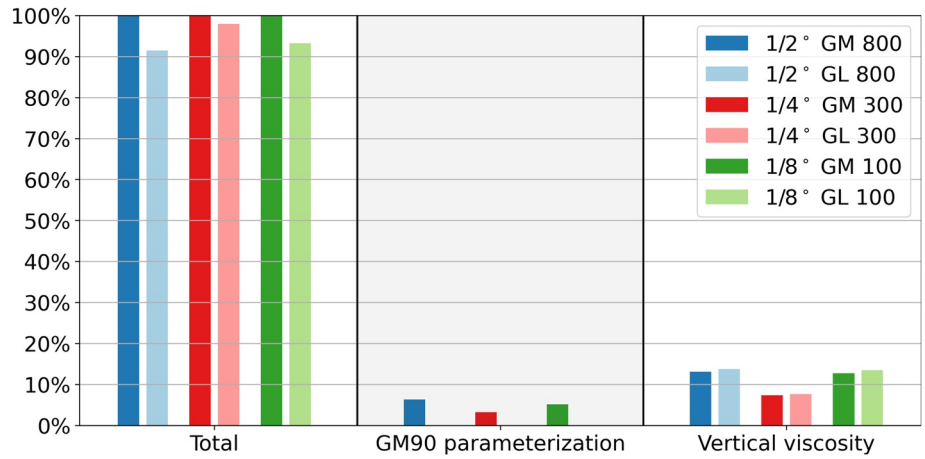

Figure 9. Comparison of runtime values for the GM90 versus GL90 simulations at 1/2° (blue bars), 1/4° (red bars), and 1/8° (green bars) grid spacing. The bars indicate the total runtime (left), runtime spent for applying GM90 in the thickness equation (middle), and runtime spent in the vertical viscosity routines (right). For each grid spacing, the bars are normalized by the total runtime of the respective GM90 simulation.

The GL90 simulations are slightly cheaper; on average, they require about 94% of the computing resources that are necessary for the GM90 simulations (Figure 9, left). The reduction in compute cost is largely explained by the fact that the GL90 experiments can skip through the routines that apply GM90 in the thickness equation, which amount to about 5% of the total runtime in the GM90 experiments (Figure 9, middle). On the other hand, the GL90 experiments require on average only 0.5% more compute time in the vertical viscosity routines than the GM90 experiments (Figure 9, right). This small additional expense is due to the (a) computation of the GL90 coupling coefficient (Equation C2) associated with ν^{GL} (Equation 26) from the κ^{GM} that is specified by the user, and (b) addition of the GL90 coupling coefficient to the coupling coefficient associated with the background vertical viscosity (Equation C1). No extra cost is imposed by the vertical viscosity solver itself; the latter is always required due to the use of a background vertical viscosity (and other vertical viscous stresses) and operates merely with a modified coupling coefficient.

5. Discussion

We have compared the GL90 and GM90 parameterizations in an idealized isopycnal coordinate model. The two parameterizations mimic the restratification effect of mesoscale eddies, but they do so in two distinct ways: GM90 via the adiabatic flattening of isopycnals, GL90 via the vertical mixing of horizontal momentum. In the following, we discuss our results from both a theoretical and practical perspective, and give an outlook for next steps.

5.1. Theoretical Considerations

We argued that common approaches to implementing the GM90 parameterization in isopycnal-layer models are inconsistent with any possible combination of non-TWA or TWA thickness, continuity, and momentum equations (Section 2). The inconsistency is partly due to the fact that the non-thickness-weighted isopycnal average conserves neither tracers nor momentum. This problem is resolved when replacing GM90 with the GL90 parameterization. GL90 provides a path for parameterizing the eddy terms in the stacked shallow water equations in a way that is fully consistent with the TWA framework. From a theoretical perspective, the GL90 parameterization provides an attractive solution for isopycnal coordinate models. Indeed, GL90 allows for a clean interpretation of what the model variables and parameterizations represent—an important property if one wants to compare coarse-resolution model output to observations or high-resolution model output, where eddy terms can be diagnosed.

5.2. GM90 Versus GL90 in Practice

The GM90 and GL90 parameterizations have profoundly different effects on the energy budget: GM90 dissipates APE, while GL90 extracts KE (Figure 7). Despite these inherently different energy pathways, we found the flow to adjust in such a way that GM90 and GL90 have almost identical effects on energy levels and vertical structure, as long as one chooses $\nu^{GL} = \kappa^{GM} f^2/N^2$. While the effective equivalence of GM90 and GL90 is expected under the assumption of geostrophy, one cannot necessarily expect geostrophy to hold everywhere, in particular for models with topography and equatorial latitudes. Our stacked shallow water model simulations spanning two hemispheres with idealized topography confirmed that, nevertheless, the effective equivalence of GM90 and GL90 holds true across non-eddying to eddy-permitting grid resolutions, and both for spatially constant κ^{GM} (Section 4) and spatially varying κ^{GM} (Figures S1–S3 in Supporting Information S1).

The only notable exception is a small discrepancy found between the 1/2° GM90 and GL90 simulations in their vertical flow structure in the tropical region - a region where geostrophy breaks down. We note that many models employ GM90 together with a resolution function (Hallberg, 2013), which mutes GM90 in the equatorial region where the deformation radius is sufficiently resolved (Figure 1). On the other hand, GL90 is essentially switched off close to the equator because $\nu^{GL} \sim f^2$. We therefore speculate that the small discrepancy noted above may not be present if we had used a resolution function in the GM90 simulations.

The similarity in the effects of GM90 and GL90 in our isopycnal coordinate model is perhaps more striking than what was found in previous studies, all of which have compared these two parameterizations in z-coordinate models (Ferreira & Marshall, 2006; McWilliams & Gent, 1994; Saenz et al., 2015; Zhao & Vallis, 2008). We conclude that in isopycnal coordinate models, the GL90 parameterization provides a promising alternative to the GM90 parameterization.

The GL90 parameterization is easy to implement because virtually every model uses a vertical viscosity solver already for other vertical processes. On the other hand, implementing GM90 in isopycnal coordinate models can be delicate near in- and outcrops; for instance, limiters are required to avoid fluxing volume out of vanished layers. Likely as a consequence of these difficulties, the coarse GM90 simulations (at 1/2° grid spacing) showed noisy surface velocities. GL90 produced noise-free flow patterns as it bypasses numerical implementation issues near the surface. While this was not the focus of our work, the reduction of grid scale noise by GL90 could also diminish spurious diapycnal mixing and allow the choice of a smaller horizontal viscosity than necessary with GM90 (Ferreira & Marshall, 2006; Zhao & Vallis, 2008).

It is also worth mentioning that vertical viscosity can be treated implicitly, which can improve the stability of the code. In terms of computational efficiency, we found that GL90 has a slight advantage because a vertical viscosity solver is employed at every timestep anyway due to other model processes. In other words, GL90 requires essentially no extra computational effort, while the GM90 routines can be entirely skipped. This computational advantage is reflected in the runtimes of our experiments: the GL90 simulations required only 94% of the compute time that was necessary for the GM90 simulations.

5.3. Outlook

An avenue for future work is to integrate GL90 into a parameterization that makes use of an explicit subgrid scale energy budget (Eden & Greatbatch, 2008; Jansen et al., 2015; Marshall & Adcroft, 2010). Having a prognostic equation for the subgrid scale energy budget is advantageous for multiple reasons, one of which is that the κ^{GM} (or, then, the ν^{GL}) coefficient can be constrained by the subgrid scale energy through a mixing length argument. The integration of GL90 into a subgrid scale energy budget parameterization is a straightforward task, which simply consists of substituting the GM work with the GL work in the subgrid scale budget. Again, we anticipate very similar solutions because we found the (online diagnosed) depth-integrated GM and GL work to have similar horizontal distributions (Figure 8). A prognostic equation for the subgrid scale energy budget could also provide energetic constraints for a backscatter parameterization (Jansen & Held, 2014; Jansen et al., 2019; Juricke et al., 2019). Comparison with offline diagnostics highlighted that our simulations would benefit from backscatter (Figure 7). Future work should examine how GL90 performs in concert with a backscatter parameterization. It will be interesting to see whether the slightly smoother velocity structure produced by GL90 enables backscatter that is more numerically stable than achieved with GM90.

Another direction for future development of the GL90 parameterization is to formulate an anisotropic version based on the anisotropic GM90 parameterization of R. D. Smith and Gent (2004). The resulting parameterization

is significantly simpler than the general anisotropic viscosity of R. D. Smith and McWilliams (2003) because only the vertical component of viscosity is horizontally anisotropic. Implementing an anisotropic version of GL90 may be much easier than implementing an anisotropic version of GM90 (R. D. Smith & Gent, 2004). On an Arakawa B-grid, implementation of such an anisotropic GL90 parameterization would be straightforward, while on a C-grid it would require some extra care.

One barrier to the widespread adoption of the GL90 approach is that turbulence parameterizations (such as bulk formulae for surface fluxes, or parameterizations of shear-driven instabilities in the mixed layer) are generally formulated in terms of the Eulerian mean flow, which is not readily available in the TWA equations. It remains an open question how challenging it would be to reformulate these parameterizations in terms of the TWA velocity, or whether a reformulation is even necessary given that the derivations of these parameterizations are typically vague about the specific definition of the "mean" flow, and noting their various other shortcomings. On the upside, the GL90 parameterization may open the door to explore related parameterizations such as those for bottom (i.e., topographic) form stresses. A parameterization for bottom form stress would very naturally enter as a boundary condition in the TWA framework and associated vertical viscosity parameterization.

In this study, we have worked within a stacked shallow water model. Moving forward, the GL90 parameterization has to be tested in more realistic isopycnal coordinate models that also include a mixed layer. A complication is that vanishing stratification in the mixed layer implies infinite vertical viscosity $\nu^{\mathrm{GL}} = f^2/N^2\, \kappa^{\mathrm{GM}}$, an issue that is analogous to the problem of infinite isopycnal slopes arising in the GM90 framework. To remedy this issue, one could potentially leverage ideas from Ferrari et al. (2010) and solve an elliptic boundary-value problem, adapted to dealing with infinite vertical viscosity rather than infinite isopycnal slopes. One advantage of GL90 is that one can solve the tridiagonal equation for vertical viscosity with an exceptionally large (almost infinite) viscosity by using implicit schemes in the vertical, for example, with the modified tridiagonal solver described by Schopf and Loughe (1995). There is no need to limit the viscosity for stability. By contrast, the horizontal GM90 scheme is handled explicitly and therefore needs bounds on the magnitude of the GM90 streamfunction.

An alternative way for employing GL90 in more realistic configurations is to focus on hybrid coordinate schemes, which are already utilized in many modern ocean general circulation models (e.g., Adcroft et al., 2019; Bleck, 2002; Bleck et al., 1992; Hofmeister et al., 2010; Ringler et al., 2013; Seland et al., 2020). In some parts of the domain hybrid coordinate schemes use an isopycnal coordinate directly analogous to the stacked shallow water equations, while in other parts of the domain they use geopotential or terrain-following coordinates. The GL90 parameterization developed here should port directly to the isopycnal coordinate part of these models, but some extra care is required to transition the parameterization from the isopycnal part of the domain to the other parts.

One approach to extending the current work to general coordinates is to discretize the general vertical coordinate and then apply the TWA machinery using general coordinate layer thickness instead of isopycnal layer thickness. One advantage of such an approach is that in regions of the model where the general coordinate layer thicknesses are uniform, the TWA reduces to the standard Reynolds average and the form stress that GL90 parameterizes is identically zero. For example, many hybrid coordinate schemes use a geopotential coordinate in the ocean surface mixed layer (Adcroft et al., 2019; Bleck, 2002). It would be natural to set the GL90 viscous coefficient to zero within the geopotential coordinate mixed layer, which avoids the difficulties associated with defining the GL90 viscosity in regions of weak stratification and with applying surface wind stress in the presence of a GL90 viscosity. Applying the TWA machinery using general coordinate layer thickness instead of isopycnal layer thickness will introduce new theoretical challenges, but may also lead to a unification of lateral physics parameterizations for general coordinate models.

Appendix A: Conservation Properties of Averaging Operators

In this section, we show that the non-thickness-weighted average is non-conservative, while the TWA is conservative.

The total tracer content is

$$C_{\mathrm{total}} = \int \sum_{n=1}^{N} h_n C_n \, \mathrm{d}A, \tag{A1}$$

where the integral is a definite integral over the horizontal extent of the spatial domain. Impermeable boundary conditions in the thickness-weighted tracer Equation 6 guarantee that total tracer content is conserved:

$$\frac{\mathrm{d}C_{\text{total}}}{\mathrm{d}t} = 0. \tag{A2}$$

However, the non-thickness-weighted average does not conserve total tracer content. If we assume that the Reynolds average commutes with the domain integral (and thus has no effect on domain-integrated quantities), then we have

$$C_{\text{total}} = \int \sum_{n=1}^{N} \overline{h_n C_n}\, \mathrm{d}A = \int \sum_{n=1}^{N} \left(\overline{h}_n \overline{C}_n + \overline{h'_n C'_n} \right) \mathrm{d}A. \tag{A3}$$

The total tracer content in the mean part of the non-thickness-weighted fields is

$$\int \sum_{n=1}^{N} \overline{h}_n \overline{C}_n \, \mathrm{d}A \neq C_{\text{total}} \tag{A4}$$

because in general the tracer content in the eddy field is nonzero. In order to maintain conservation of total tracer content, the non-thickness-weighted equations must account for exchange of tracer between the mean and eddy fields, and this is reflected in the fact that the eddy terms are non-conservative. The evolution equation for the total tracer content in the mean part of the non-thickness-weighted fields is derived by integrating the following

$$\partial_t \left(\bar{h}_n \bar{C}_n \right) + \nabla \cdot \left(\bar{h}_n \bar{\boldsymbol{u}}_n \bar{C}_n \right) = -\bar{C}_n \nabla \cdot \left(\overline{h'_n \boldsymbol{u}'_n} \right) - \bar{h}_n \overline{\boldsymbol{u}'_n \cdot \nabla C'_n} \tag{A5}$$

and summing over layers, assuming impermeable boundary conditions on $\bar{\boldsymbol{u}}_n$:

$$\frac{\mathrm{d}}{\mathrm{d}t} \int \sum_{n=1}^{N} \bar{h}_n \bar{C}_n \, \mathrm{d}A = -\int \sum_{n=1}^{N} \left[\bar{C}_n \nabla \cdot \left(\overline{h'_n \boldsymbol{u}'_n} \right) + \bar{h}_n \overline{\boldsymbol{u}'_n \cdot \nabla C'_n} \right] \mathrm{d}A \neq 0. \tag{A6}$$

A similar analysis can be carried out for the total momentum, $\int \sum_n h_n \boldsymbol{u}_n \mathrm{d}A$, showing that the non-thickness-weighted eddy field has a nonzero momentum content, which is reflected in the fact that the eddy terms in the non-thickness-weighted velocity Equation 10 are non-conservative.

In contrast, the TWA preserves the total quantity of tracers as well as total momentum. For example, considering total tracer content, the total tracer content in the mean part of the thickness-weighted fields is

$$\int \sum_{n=1}^{N} \overline{h}_n \widehat{C}_n \, \mathrm{d}A = \int \sum_{n=1}^{N} \overline{h}_n \frac{\overline{h_n C_n}}{\overline{h}_n} \, \mathrm{d}A = \int \sum_{n=1}^{N} \overline{h_n C_n} \, \mathrm{d}A = C_{\text{total}}, \tag{A7}$$

where the last step assumes that the Reynolds average commutes with integrals. The total tracer content in the eddy part of the thickness-weighted fields is therefore zero, and similar conclusions result for momentum by swapping C_n with $\boldsymbol{u}_n$. Because of this property, the eddy terms in the thickness-weighted tracer and velocity equations are conservative; unlike in the non-thickness-weighted case, they do not need to account for exchanges between the resolved and unresolved reservoirs of total tracer and momentum.

Appendix B: Connecting GL90 to Eddy Interfacial Form Stress

The pressure force acting on an arbitrary fluid region, $\mathcal{R}$, can be written in two equivalent manners

$$-\int_{\mathcal{R}} \nabla p \, \mathrm{d}V = -\oint_{\partial \mathcal{R}} p \, \hat{\boldsymbol{n}} \, \mathrm{d}S, \tag{B1}$$

with this identity following from the divergence theorem, and with $\hat{\boldsymbol{n}}$ the outward unit normal vector on the region boundary, $\partial \mathcal{R}$. The left hand side is the volume integral of the pressure gradient body force acting throughout the region, whereas the right hand side is the area integral of the pressure contact force acting on the region boundary. In a hydrostatic fluid, the vertical portion of the pressure force balances the weight of fluid, whereas the horizontal portion gives rise to horizontal acceleration. Pressure form stress refers to the horizontal projection of the force per unit area from pressure that acts on a surface whose outward normal has a nonzero projection in both the horizontal and vertical directions. That is, there is only a pressure form stress on a sloping surface. We illustrate these points for a shallow water fluid in Figure B1.

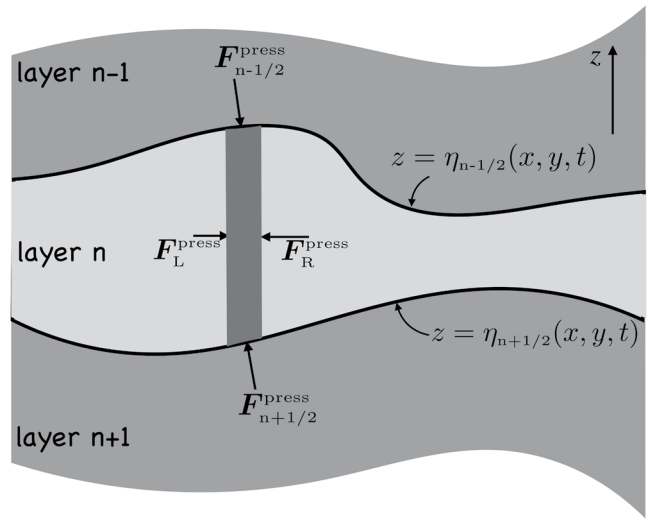

Figure B1. A schematic of the contact pressure force per area acting on the boundaries of a vertical column region within a shallow water layer of density ρ_n. Since fluid moves as vertical columns in a shallow water layer, we focus on the pressure forces acting on this column. The interface at the lower boundary is at the vertical position $z = \eta_{n+1/2}$, and the upper interface is at $z = \eta_{n-1/2}$. In accordance with Newton's third law (and since we ignore surface tension), pressures are continuous across each of the $\eta_{n\pm1/2}$ layer interfaces so that the pressure forces are equal in magnitude yet oppositely directed on the opposite sides to the interfaces. The layer thickness is the difference between the interface positions, $h_n = \eta_{n-1/2} - \eta_{n+1/2}$. The boundaries of the columnar region feel a contact pressure force from the surrounding fluid that acts inward (compressive). The left side of the column experiences a pressure p_L; the right side experiences p_R; the upper interface has a pressure $p_{n-1/2}$ acting between the layer $n-1$ and layer n, and the lower interface has a pressure $p_{n+1/2}$ acting between the layer $n+1$ and layer n. The net pressure acting on the column is computed as the area integral of the pressure acting around the full extent of the column boundaries. The horizontal components of the pressure acting on the top and bottom interfaces are the interfacial form stresses.

The fundamental assumption of the GL90 parameterization is that mesoscale eddies provide a vertically downgradient transfer of horizontal momentum through the action of eddy induced pressure form stresses. For the shallow water fluid, pressure form stresses act on the interfaces between shallow water fluid layers, in which case they are referred to as interfacial form stresses. In this appendix, we expose the basic features of interfacial form stress for the shallow water fluid, thus further describing how the GL90 parameterization appears in a shallow water fluid.

B1. Shallow Water Pressure Identities

We make use of the following relations holding for the hydrostatic pressure within a shallow water layer, p_n, and the pressure at a layer interface, $p_{n\pm1/2}$

$$h_n = \eta_{n-1/2} - \eta_{n+1/2} \tag{B2a}$$

$$p_n = p_{n-1/2} + g\,\rho_n\left(\eta_{n-1/2} - z\right) = \left(p_{n-1/2} + g\,\rho_n\,\eta_{n-1/2}\right) - g\,\rho_n\,z \tag{B2b}$$

$$g\,\rho_n\,h_n = p_{n+1/2} - p_{n-1/2} = g\,\rho_n\left(\eta_{n-1/2} - \eta_{n+1/2}\right) \tag{B2c}$$

$$p_{1/2} = p_{\text{a}}, \tag{B2d}$$

with $p_{\text{a}}(x, y, t)$ the applied (or atmospheric) pressure at the ocean surface, which is set to zero in our simulations. The interfacial pressures, $p_{n\pm1/2}(x, y, t)$, and interfacial heights, $\eta_{n\pm1/2}(x, y, t)$, are functions of horizontal position and time, and as such so too are the layer thickness, $h_n(x, y, t)$ whereas the densities, ρ_n, are constant within each layer.

The layer pressure, $p_n(x, y, z, t)$, in Equation B2b is a linear function of vertical position through the term $-g\,\rho_n\,z$. This term has a zero horizontal gradient so that $\nabla_z p_n$ is independent of depth within a shallow water layer.

Hence, when working with the pressure gradient force we can choose to drop the $g\,\rho_n\,z$ term and instead use the Montgomery potential (Equation 5)

$$M_n = p_n + g\,\rho_n\,z \quad \text{with} \quad \nabla M_n = \nabla_z p_n. \tag{B3}$$

See also Vallis (2017) in his Equation 3.44, where he refers to M_n as the "dynamic pressure." However, just for this appendix we find it more convenient to work with p_n since doing so facilitates physically interpreting the transformation between the body force and contact force versions of the pressure force as in Equation B1. Note that in Equation B3 we exposed the z label on the horizontal gradient operator, which adds clarity since p_n is a function of z within a layer.

B2. Exposing the Interfacial Pressure Form Stress

The thickness-weighted horizontal pressure gradient, as found in the thickness-weighted momentum Equation 7, can be decomposed as

$$-h_n \nabla_z p_n = -\nabla P_n + \boldsymbol{F}_n^{\text{form}}, \tag{B4}$$

where on the left hand side we expose the subscript on the gradient operator,∇_z, since p_n is a function of z, whereas this extra notation is not needed on the right hand side since all terms are vertically constant within a layer. The first right hand side term in Equation B4 results from vertically integrating pressure over a shallow water layer

$$P_n = \int_{\eta_{n+1/2}}^{\eta_{n-1/2}} p_n(z)\,\mathrm{d}z = h_n \left(\frac{g\,\rho_n\,h_n}{2} + p_{n-1/2} \right), \tag{B5}$$

with its negative horizontal gradient given by

$$-\nabla P_n = -\left(h_n\,\nabla p_{n+1/2} + p_{n-1/2}\,\nabla h_n \right). \tag{B6}$$

The second horizontal stress in Equation B4 is the interfacial form stress acting on sloping upper and lower interfaces to the layer,

$$\boldsymbol{F}_n^{\text{form}} = p_{n-1/2} \nabla \eta_{n-1/2} - p_{n+1/2} \nabla \eta_{n+1/2}. \tag{B7}$$

The interfacial form stress provides an inviscid exchange of horizontal momentum between shallow water layers, and it does so in a manner consistent with Newton's third law. Correspondingly, the column sum of the interfacial form stress arises just from form stresses active at the ocean surface and ocean bottom

$$\sum_{n=1}^{N} \boldsymbol{F}_n^{\text{form}} = p_{\text{a}} \nabla \eta - p_{\text{b}} \nabla \eta_{\text{b}}, \tag{B8}$$

where $z = \eta(x, y, t)$ is the free surface and $z = \eta_{\text{b}}(x, y) = -D(x, y)$ is the ocean bottom.

B3. Connecting Eddy Interfacial Form Stress to GL90

Following Section 3 of Greatbatch (1998), we make use of the decomposition (Equation B4) to render the mean thickness-weighted pressure gradient

$$-\overline{h_n\,\nabla p_n} = -\overline{h}_n\,\nabla \overline{p}_n - \overline{h_n}\,\widehat{\nabla p'_n} = -\nabla \overline{P_n} + \overline{\boldsymbol{F}_n^{\text{form}}}, \tag{B9}$$

which can be written

$$-\overline{h_n\,\nabla p_n} = -\overline{h}_n\,\nabla \overline{p}_n - \overline{\nabla P'_n} + \overline{\boldsymbol{F}_n^{\text{form}'}}, \tag{B10}$$

with the eddy contributions given by

$$-\left[\overline{h_n}\,\widehat{\nabla p'_n}\right]_{\text{P-contribution}} = -\overline{\nabla P'_n} = -\overline{h'_n\,\nabla p'_{n+1/2}} - \overline{p'_{n-1/2}\,\nabla h'_n}, \tag{B11a}$$

$$-\left[\overline{h_n}\ \widehat{\nabla p'_n}\right]_{\text{eddy form-stress}} = \overline{\boldsymbol{F}_n^{\text{form}'}} = \overline{p'_{n-1/2}\ \nabla\eta'_{n-1/2}} - \overline{p'_{n+1/2}\ \nabla\eta'_{n+1/2}}. \tag{B11b}$$

Greatbatch (1998) argues that for geostrophic eddies, the term $-\overline{\nabla P'_n}$ is negligible relative to the eddy interfacial form stress, $\overline{\boldsymbol{F}_n^{\text{form}'}}$, thus motivating a focus on developing a parameterization of eddy form stress. In turn, the GL90 parameterization assumes that the mean action from mesoscale eddy induced form stress leads to a vertical downgradient transfer of horizontal momentum. This assumption then motivates the GL90 parameterization of $\overline{\boldsymbol{F}_n^{\text{form}'}}$ as detailed in Section 3.

Appendix C: Implementation of GL90 in MOM6

MOM6 handles vertical mixing of momentum fully implicitly, a necessity to allow for vanishingly small layers. Inputs into the tridiagonal solver for the implicit vertical viscosity scheme are coupling coefficients of the form

$$a^u_{n-1/2} = \frac{2\nu_{n-1/2}\Delta t}{h^u_{n-1} + h^u_n}, \quad a^v_{n-1/2} = \frac{2\nu_{n-1/2}\Delta t}{h^v_{n-1} + h^v_n}, \tag{C1}$$

which are located at zonal $\left(a^u_{n-1/2}\right)$ and meridional $\left(a^v_{n-1/2}\right)$ velocity points and layer interfaces (e.g., Schopf & Loughe, 1995). The thicknesses at velocity points, h^u_n, h^v_n are computed as an average of the thicknesses of the two adjacent grid cells, with an upwind biased estimate near the bottom. We leverage the existing implicit vertical solver (including its numerical stability) and choose the following "non-invasive" approach. We simply calculate additional coupling coefficients that are associated with the GL90 parameterization, $a^{\text{GL},u}_{n-1/2}, a^{\text{GL},v}_{n-1/2}$. The sums of the coupling coefficients,

$$a^u_{n-1/2} + a^{\text{GL},u}_{n-1/2}, \qquad a^v_{n-1/2} + a^{\text{GL},v}_{n-1/2},$$

are then inserted into the vertical viscosity scheme; the vertical viscosity scheme itself is not altered.

The coupling coefficients associated with the GL90 parameterization have the form

$$a^{\text{GL},[u,v]}_{n-1/2} = \frac{\kappa^{\text{GM}}_{n-1/2}\ f^2\Delta t}{g'_{n-1/2}} \cdot (1 - b(\tilde{z})). \tag{C2}$$

The fraction on the right hand side of Equation C2 is obtained when applying Equation C1 to the expression of the GL90 vertical viscosity (Equation 26). The factor $(1 - b(\tilde{z}))$ has the purpose to avoid fluxing momentum into vanished layers near the bottom. b is a taper function of the form $b(\tilde{z}) = \left(1 + 0.09 \cdot \tilde{z}^6\right)^{-1}$, where $\tilde{z} = (z + D)/\Delta h_{\text{BBL,GL}}$ is the normalized distance from the ocean bottom, with tunable parameter $\Delta h_{\text{BBL,GL}}$. The factor $(1 - b(\tilde{z}))$ is 0 within $\Delta h_{\text{GL,BBL}} - \varepsilon$ from the bottom, and 1 for distances greater than $\Delta h_{\text{GL,BBL}} + \varepsilon$ from the bottom, for small $\varepsilon > 0$, with a smooth transition in between. In practice, $z + D$ is computed as the sum of cell thicknesses, accumulated from the bottom upwards. Note that $b(\tilde{z})$ is needed at u- and v-velocity points; to obtain the thicknesses at velocity points, we compute an upwind biased estimate (i.e., harmonic mean) from the thicknesses of the two adjacent grid cells.

The factor $(1 - b(\tilde{z}))$ in Equation C2 is necessary. Skipping this factor can lead to spurious large bottom velocities over the continental slope (Figure C1c). If the factor $(1 - b(\tilde{z}))$ is skipped, the large vertical gradient in the GL90 coupling coefficient near the bottom facilitates occasional upslope thickness transport into near-vanished layers. The upslope layer then drains slowly (over several days to weeks), leading to strong downslope velocities near the bottom while the layer is draining. The factor $(1 - b(\tilde{z}))$ effectively mutes the GL90 scheme in vanished bottom layers and the problem of spurious bottom velocities is remedied (Figures C1d–C1h). All GL90 simulations presented outside of this appendix use $\Delta h_{\text{GL,BBL}} = 5$ m.

It is important to note that the GL90 scheme is not sensitive to the choice of $\Delta h_{\text{GL,BBL}}$, as long as $\Delta h_{\text{GL,BBL}}$ is set within a reasonable range: large enough to contain vanished layers over topography, and small enough to not contaminate the action of GL90 in the interior. We have tested values of $\Delta h_{\text{GL,BBL}} = 1$ m, 5 m, 10 m, 20 m, as well

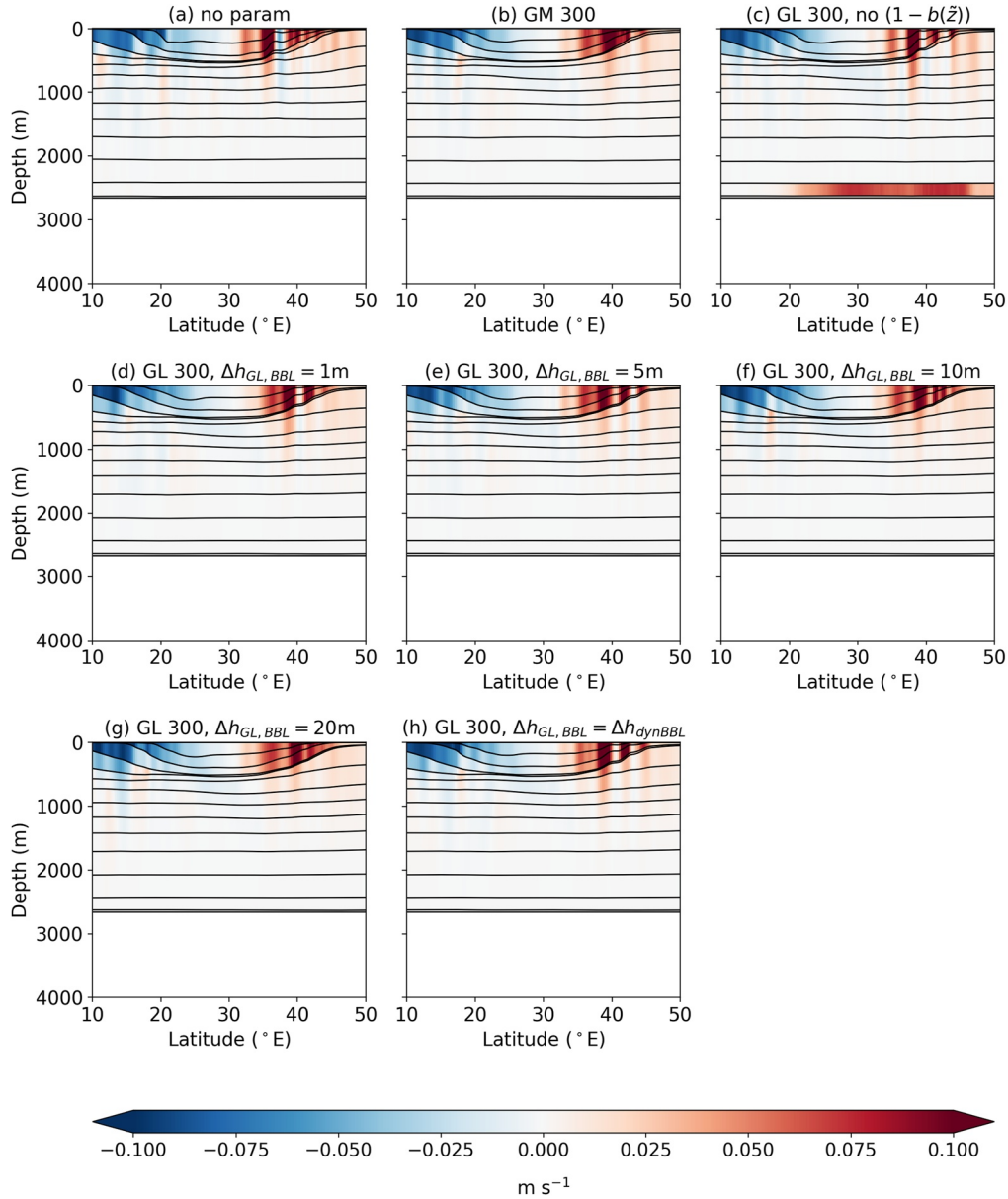

Figure C1. 2,000-day averages of zonal velocity along a south-north transect at 4°E for multiple experiments, all at 1/4° horizontal grid spacing: (a) unparameterized, (b) using GM90 with $\kappa^{GM} = 300$ m^2 s^{-1}, (c) using GL90 with $\nu^{GL} = 300 \cdot f^2/N^2$ m^2 s^{-1}, where the factor $(1 - b(\tilde{z}))$ in Equation C2 is skipped, (d)–(h) using GL90 with $\nu^{GL} = 300 \cdot f^2/N^2$ m^2 s^{-1} and different choices of $\Delta h_{GL,BBL}$.

as $\Delta h_{GL,BBL} = \Delta h_{dynBBL}$, where Δh_{dynBBL} is a dynamically computed and spatially varying bottom boundary layer thickness, and found no sensitivity of the flow and the APE to the choice of $\Delta h_{GL,BBL}$ (Figures C1 and C2). Note that skipping the factor $(1 - b(\tilde{z}))$ leads to an APE that is more than 10% larger than the APE in the corresponding GM90 simulation (yellow vs. green line, Figure C2), whereas GL90 simulations in which $a_n^{GL,[u,v]}$ is muted within $\Delta h_{GL,BBL}$ from the bottom produce virtually identical APE values as the GM90 simulation (pink lines vs. green line, Figure C2). The elevated APE in the former case is again explained by the spurious bottom velocities; a strong vertical shear is related to more tilted interfaces, via thermal wind balance.

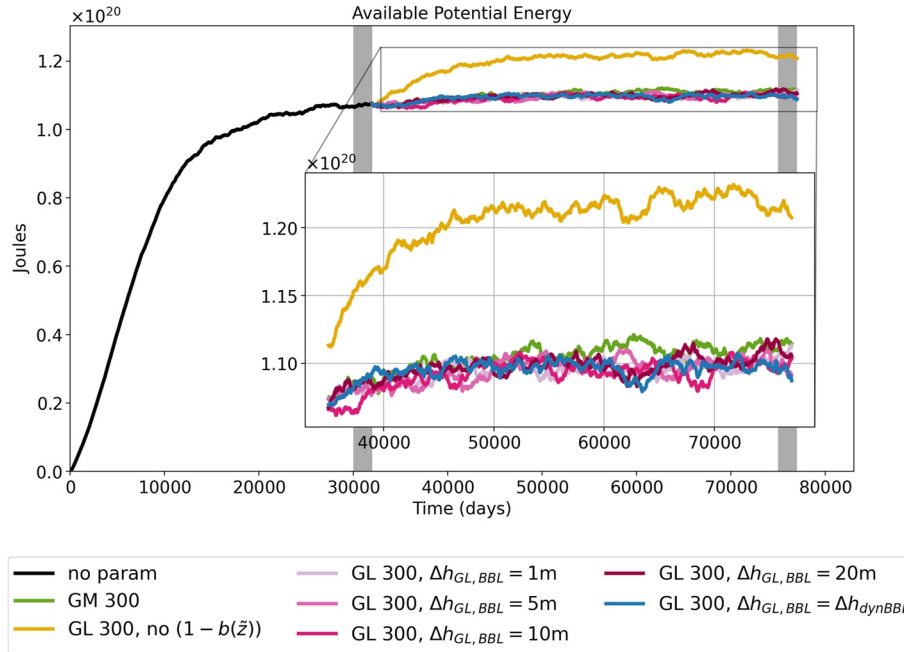

Figure C2. Timeseries of available potential energy for the eight experiments shown in Figure C1, during spin-up and equilibration. The gray shading marks the 2,000-day windows that were used for time-averaging in Figure C1.

Appendix D: GL90 in Isopycnal Versus *Z*-Coordinates

The isopycnal coordinate derivation in Section 3 differs qualitatively from the derivations by Ferreira and Marshall (2006) and Zhao and Vallis (2008), who use z-coordinates. We here review the derivation of Zhao and Vallis (2008) and thereafter discuss the differences with the isopycnal approach.

The Reynolds-averaged velocity equation in z-coordinates is

$$\frac{D\bar{\boldsymbol{u}}}{Dt} + \nabla \cdot \left(\overline{\boldsymbol{u}' \otimes \boldsymbol{u}'}\right) + f \times \bar{\boldsymbol{u}} = -\nabla\bar{\phi} + \partial_z \boldsymbol{\tau}_m, \tag{D1}$$

where D/Dt denotes the material derivative, ϕ the pressure (divided by the Boussinesq reference density), and $\boldsymbol{\tau}_m$ mechanical stresses. The Reynolds stress is the only eddy term in this equation.

The mean buoyancy, $\bar{b} = -g\bar{\rho}/\rho_0$, in a Reynolds-averaged z-coordinate Boussinesq model is shown by Zhao and Vallis (2008) to be advected by the residual mean velocity

$$\tilde{\boldsymbol{u}} = \bar{\boldsymbol{u}} + \boldsymbol{u}^*, \tag{D2}$$

where the eddy-induced velocity is

$$\boldsymbol{u}^* = -\nabla \times \left(\frac{\overline{\boldsymbol{u}'b'} \times \nabla\bar{b}}{|\nabla\bar{b}|^2}\right). \tag{D3}$$

Adding $f \times \boldsymbol{u}^*$ to both sides of Equation D1 leads to

$$\frac{D\bar{\boldsymbol{u}}}{Dt} + \nabla \cdot \left(\overline{\boldsymbol{u}' \otimes \boldsymbol{u}'}\right) + f \times \tilde{\boldsymbol{u}} = -\nabla\bar{\phi} + \partial_z \boldsymbol{\tau}_m - f \times \left[\nabla \times \left(\frac{\overline{\boldsymbol{u}'b'} \times \nabla\bar{b}}{|\nabla\bar{b}|^2}\right)\right]. \tag{D4}$$

At this point, we do not have a closed set of equations, as Equation D4 contains both the Eulerian and residual mean velocities.

To obtain an evolution equation for the residual mean velocity, Zhao and Vallis (2008) replace $D\bar{\boldsymbol{u}}/Dt$ by $D\tilde{\boldsymbol{u}}/Dt$ in equation (Equation D4). Following Section 5 of Greatbatch (1998), this replacement is justified by a geostrophic argument: as long as $D\boldsymbol{u}^*/Dt$ is order Rossby number smaller than $f \times \boldsymbol{u}^*$ then the replacement of $D\bar{\boldsymbol{u}}/Dt$ by $D\tilde{\boldsymbol{u}}/Dt$ introduces only an order-Rossby error in Equation D4. The resulting evolution equation for the residual mean velocity is

$$\frac{D\tilde{\boldsymbol{u}}}{Dt} + \nabla \cdot \left(\overline{\boldsymbol{u}' \otimes \boldsymbol{u}'}\right) + f \times \tilde{\boldsymbol{u}} = -\nabla\bar{\phi} + \partial_z \boldsymbol{\tau}_m - f \times \left[\nabla \times \left(\frac{\overline{\boldsymbol{u}' b'} \times \nabla \bar{b}}{|\nabla \bar{b}|^2}\right)\right]. \tag{D5}$$

The rightmost expression in this new equation is an eddy term that needs to be parameterized, and Zhao and Vallis (2008) show how it can be reduced by a series of approximations to a vertical mixing of momentum with viscous coefficient $\kappa^{\mathrm{GM}} f^2/N^2$.

One difference in the isopycnal versus z-coordinate derivations is that the z-coordinate approaches of Ferreira and Marshall (2006) and Zhao and Vallis (2008) rely on a geostrophic approximation (replace $D\bar{\boldsymbol{u}}/Dt$ by $D\tilde{\boldsymbol{u}}/Dt$) to obtain an equation for the residual mean velocity, whereas the TWA Equation 15 for $\hat{\boldsymbol{u}}$ is derived without any approximations (a point also emphasized by Young (2012)).

Another difference is that although the residual mean velocity, $\tilde{\boldsymbol{u}}$, advects buoyancy, it is not immediately clear why it should also advect other tracers, though that connection can be made with further effort (Bachman et al., 2020; Plumb & Ferrari, 2005). In contrast, it is clear from Equation 14 that the TWA velocity $\hat{\boldsymbol{u}}$ advects all tracers.

A final key difference is the interpretation of the residual mean velocity $\tilde{\boldsymbol{u}}$ in one formulation and the TWA velocity $\hat{\boldsymbol{u}}$ in the other. One obstacle to the widespread adoption of the residual-mean formulation of Ferreira and Marshall (2006) and Zhao and Vallis (2008) in z-coordinates is the conflict between the two interpretations of the model velocity—Eulerian versus residual mean—in different parts of an ocean model. The TWA formulation does not suffer from this problem: If the Reynolds average $\bar{\cdot}$ is loosely understood to represent a spatial averaging operator, as appropriate in any discussion of subgrid-scale parameterization, then the TWA velocity $\hat{\boldsymbol{u}}$ corresponds to the velocity instantaneously averaged in space over an isopycnal layer whose spatial mean location is known. This interpretation corresponds naturally with the finite-volume approach used in many numerical ocean models (e.g., Griffies et al., 2020), although the correspondence is not precise because the Reynolds average used here is only a formal mathematical tool whose properties are easier to manage than those of a spatial filter. In contrast, the residual mean velocity in the z-coordinate formulation is the sum of a Eulerian mean velocity plus the eddy-induced velocity (Equation D3). The eddy-induced velocity is somewhat problematic in that it is not in general equal to a velocity that has been averaged over any known location, although the residual mean velocity can be shown to approximate the TWA velocity for small-amplitude perturbations (McDougall & McIntosh, 2001; Tréguier et al., 1997).

Data Availability Statement

The parameter settings for the NeverWorld2 experiments used in this paper as well as Jupyter Notebooks for analysis are available on GitHub (Loose, 2023). The data and configuration for the unparameterized NeverWorld2 reference simulations are described in Marques et al. (2022).

Acknowledgments
We thank all members of the Ocean Transport and Eddy Energy Climate Process Team for helpful discussions and their support throughout this project. In particular, we thank Wenda Zhang for his useful comments on this manuscript. We also thank Aleksi Nummelin for sharing insights on the implementation of GM90 in the Bergen Layered Ocean Model. We are grateful to Peter Gent and three more anonymous reviewers for their useful and encouraging comments. NL and IG are supported by NSF Grant OCE 1912332. GMM and SB are supported by NSF award OCE 1912420. MFJ is supported by NSF award OCE 1912163. AA is supported by award NA18OAR4320123, from the National Oceanic and Atmospheric Administration (NOAA), U.S. Department of Commerce. SMG and RWH acknowledge support from the NOAA Geophysical Fluid Dynamics Laboratory. The statements, findings, conclusions, and recommendations are those of the author(s) and do not necessarily reflect the views of the NOAA, or the U.S. Department of Commerce. This material is also based upon work supported by the National Center for Atmospheric Research (NCAR), which is a major facility sponsored by the NSF under cooperative agreement no. 1852977. Computing and data storage resources, including the Cheyenne supercomputer, were provided by the Computational and Information Systems Laboratory at NCAR, under NCAR/CISL project number UNYU0004.

References

Adcroft, A., Anderson, W., Balaji, V., Blanton, C., Bushuk, M., Dufour, C. O., et al. (2019). The GFDL global ocean and sea ice model OM4.0: Model description and simulation features. *Journal of Advances in Modeling Earth Systems*, *11*(10), 3167–3211. https://doi.org/10.1029/2019MS001726

Bachman, S. D. (2019). The GM + E closure: A framework for coupling backscatter with the Gent and McWilliams parameterization. *Ocean Modelling*, *136*, 85–106. https://doi.org/10.1016/j.ocemod.2019.02.006

Bachman, S. D., Fox-Kemper, B., & Bryan, F. O. (2020). A diagnosis of anisotropic eddy diffusion from a high-resolution global ocean model. *Journal of Advances in Modeling Earth Systems*, *12*(2), e2019MS001904. https://doi.org/10.1029/2019MS001904

Bleck, R. (2002). An oceanic general circulation model framed in hybrid isopycnic-Cartesian coordinates. *Ocean Modelling*, *4*(1), 55–88. https://doi.org/10.1016/s1463-5003(01)00012-9

Bleck, R., Rooth, C., Hu, D., & Smith, L. T. (1992). Salinity-driven thermocline transients in a wind-and thermohaline-forced isopycnic coordinate model of the North Atlantic. *Journal of Physical Oceanography*, *22*(12), 1486–1505. https://doi.org/10.1175/1520-0485(1992)022<1486:sdttia>2.0.co;2

Computational And Information Systems Laboratory. (2017). *Cheyenne: Sgi ice xa cluster*. UCAR/NCAR. https://doi.org/10.5065/D6RX99HX
Danabasoglu, G., McWilliams, J. C., & Gent, P. R. (1994). The role of mesoscale tracer transports in the global ocean circulation. *Science*, *264*(5162), 1123–1126. https://doi.org/10.1126/science.264.5162.1123
de La Lama, M. S., LaCasce, J. H., & Fuhr, H. K. (2016). The vertical structure of ocean eddies. *Dynamics and Statistics of the Climate System*, *1*(1), dzw001. https://doi.org/10.1093/climsys/dzw001
Eden, C., & Greatbatch, R. J. (2008). Towards a mesoscale eddy closure. *Ocean Modelling*, *20*(3), 223–239. https://doi.org/10.1016/j.ocemod.2007.09.002
Ferrari, R., Griffies, S. M., Nurser, A. J. G., & Vallis, G. K. (2010). A boundary-value problem for the parameterized mesoscale eddy transport. *Ocean Modelling*, *32*(3), 143–156. https://doi.org/10.1016/j.ocemod.2010.01.004
Ferreira, D., & Marshall, J. (2006). Formulation and implementation of a "residual-mean" ocean circulation model. *Ocean Modelling*, *13*(1), 86–107. https://doi.org/10.1016/j.ocemod.2005.12.001
Gent, P. R. (2011). The Gent–McWilliams parameterization: 20/20 hindsight. *Ocean Modelling*, *39*(1), 2–9. https://doi.org/10.1016/j.ocemod.2010.08.002
Gent, P. R., & McWilliams, J. C. (1990). Isopycnal mixing in ocean circulation models. *Journal of Physical Oceanography*, *20*(1), 150–155. https://journals.ametsoc.org/view/journals/phoc/20/1/1520-0485_1990_020_0150_imiocm_2_0_co_2.xml
Gent, P. R., Willebrand, J., McDougall, T. J., & McWilliams, J. C. (1995). Parameterizing eddy-induced tracer transports in ocean circulation models. *Journal of Physical Oceanography*, *25*(4), 463–474. https://doi.org/10.1175/1520-0485(1995)025⟨0463:PEITTI⟩2.0.CO;2
Greatbatch, R. J. (1998). Exploring the relationship between eddy-induced transport velocity, vertical momentum transfer, and the isopycnal flux of potential vorticity. *Journal of Physical Oceanography*, *28*(3), 422–432. https://doi.org/10.1175/1520-0485(1998)028⟨0422:ETRBEI⟩2.0.CO;2
Greatbatch, R. J., & Lamb, K. G. (1990). On parameterizing vertical mixing of momentum in non-eddy resolving ocean models. *Journal of Physical Oceanography*, *20*(10), 1634–1637. https://journals.ametsoc.org/view/journals/phoc/20/10/1520-0485_1990_020_1634_opvmom_2_0_co_2.xml?tab_body=abstract-display
Griffies, S. M. (1998). The Gent–McWilliams skew flux. *Journal of Physical Oceanography*, *28*(5), 831–841. https://doi.org/10.1175/1520-0485(1998)028⟨0831:TGMSF⟩2.0.CO;2
Griffies, S. M. (2004). *Fundamentals of ocean climate models*. Princeton University Press.
Griffies, S. M., Adcroft, A., & Hallberg, R. W. (2020). A primer on the vertical Lagrangian-remap method in ocean models based on finite volume generalized vertical coordinates. *Journal of Advances in Modeling Earth Systems*, *12*(10). https://doi.org/10.1029/2019MS001954
Griffies, S. M., Danabasoglu, G., Durack, P. J., Adcroft, A. J., Balaji, V., Böning, C. W., et al. (2016). Omip contribution to CMIP6: Experimental and diagnostic protocol for the physical component of the Ocean Model Intercomparison Project. *Geoscientific Model Development*, *9*, 3231–3296. https://doi.org/10.5194/gmd-9-3231-2016
Griffies, S. M., & Hallberg, R. W. (2000). Biharmonic friction with a Smagorinsky-like viscosity for use in large-scale eddy-permitting ocean models. *Monthly Weather Review*, *128*(8), 2935–2946. https://doi.org/10.1175/1520-0493(2000)128⟨2935:BFWASL⟩2.0.CO;2
Hallberg, R. (2013). Using a resolution function to regulate parameterizations of oceanic mesoscale eddy effects. *Ocean Modelling*, *72*, 92–103. https://doi.org/10.1016/j.ocemod.2013.08.007
Hofmeister, R., Burchard, H., & Beckers, J.-M. (2010). Non-uniform adaptive vertical grids for 3D numerical ocean models. *Ocean Modelling*, *33*(1–2), 70–86. https://doi.org/10.1016/j.ocemod.2009.12.003
Jansen, M. F., Adcroft, A., Khani, S., & Kong, H. (2019). Toward an energetically consistent, resolution aware parameterization of ocean mesoscale eddies. *Journal of Advances in Modeling Earth Systems*, *11*(8), 2844–2860. https://doi.org/10.1029/2019MS001750
Jansen, M. F., Adcroft, A. J., Hallberg, R., & Held, I. M. (2015). Parameterization of eddy fluxes based on a mesoscale energy budget. *Ocean Modelling*, *92*, 28–41. https://doi.org/10.1016/j.ocemod.2015.05.007
Jansen, M. F., & Held, I. M. (2014). Parameterizing subgrid-scale eddy effects using energetically consistent backscatter. *Ocean Modelling*, *80*, 36–48. https://doi.org/10.1016/j.ocemod.2014.06.002
Johnson, G. C., & Bryden, H. L. (1989). On the size of the Antarctic Circumpolar Current. *Deep-Sea Research, Part A: Oceanographic Research Papers*, *36*(1), 39–53. https://doi.org/10.1016/0198-0149(89)90017-4
Juricke, S., Danilov, S., Koldunov, N., Oliver, M., Sein, D., Sidorenko, D., & Wang, Q. (2020). A kinematic kinetic energy backscatter parametrization: From implementation to global ocean simulations. *Journal of Advances in Modeling Earth Systems*, *12*(12), e2020MS002175. https://doi.org/10.1029/2020ms002175
Juricke, S., Danilov, S., Kutsenko, A., & Oliver, M. (2019). Ocean kinetic energy backscatter parametrizations on unstructured grids: Impact on mesoscale turbulence in a channel. *Ocean Modelling*, *138*, 51–67. https://doi.org/10.1016/j.ocemod.2019.03.009
Kent, J., Whitehead, J. P., Jablonowski, C., & Rood, R. B. (2014). Determining the effective resolution of advection schemes. Part I: Dispersion analysis. *Journal of Computational Physics*, *278*, 485–496. https://doi.org/10.1016/j.jcp.2014.01.043
Kjellsson, J., & Zanna, L. (2017). The impact of horizontal resolution on energy transfers in global ocean models. *Fluids*, *2*(3), 45. https://doi.org/10.3390/fluids2030045
Loose, N. (2023). Noraloose/gl90paper: V1.0.0 [Software]. Zenodo. https://doi.org/10.5281/zenodo.8193330
Loose, N., Bachman, S., Grooms, I., & Jansen, M. (2022). Diagnosing scale-dependent energy cycles in a high-resolution isopycnal ocean model. *Journal of Physical Oceanography*, *53*(1), 157–176. https://doi.org/10.1175/JPO-D-22-0083.1
Marques, G. M., Loose, N., Yankovsky, E., Steinberg, J. M., Chang, C.-Y., Bhamidipati, N., et al. (2022). NeverWorld2: An idealized model hierarchy to investigate ocean mesoscale eddies across resolutions [Dataset]. Geoscientific Model Development, *15*(17), 6567–6579. https://doi.org/10.5194/gmd-15-6567-2022
Marshall, D. P., & Adcroft, A. J. (2010). Parameterization of ocean eddies: Potential vorticity mixing, energetics and Arnold's first stability theorem. *Ocean Modelling*, *32*(3), 188–204. https://doi.org/10.1016/j.ocemod.2010.02.001
McDougall, T. J., & McIntosh, P. C. (2001). The temporal-residual-mean velocity. Part II: Isopycnal interpretation and the tracer and momentum equations. *Journal of Physical Oceanography*, *31*(5), 1222–1246. https://doi.org/10.1175/1520-0485(2001)031⟨1222:TTRMVP⟩2.0.CO;2
McWilliams, J. C., & Gent, P. R. (1994). The wind-driven ocean circulation with an isopycnal-thickness mixing parameterization. *Journal of Physical Oceanography*, *24*(1), 46–65. https://doi.org/10.1175/1520-0485(1994)024⟨0046:TWDOCW⟩2.0.CO;2
Munk, W. H., & Palmén, E. (1951). Note on the dynamics of the Antarctic Circumpolar Current. *Tellus*, *3*(1), 53–55. https://doi.org/10.3402/tellusa.v3i1.8609
Plumb, R. A., & Ferrari, R. (2005). Transformed Eulerian-mean theory. Part I: Nonquasigeostrophic theory for eddies on a zonal-mean flow. *Journal of Physical Oceanography*, *35*(2), 165–174. https://doi.org/10.1175/JPO-2669.1
Rhines, P. B., & Young, W. R. (1982). Homogenization of potential vorticity in planetary gyres. *Journal of Fluid Mechanics*, *122*(-1), 347–367. https://doi.org/10.1017/S0022112082002250

Ringler, T., Petersen, M., Higdon, R. L., Jacobsen, D., Jones, P. W., & Maltrud, M. (2013). A multi-resolution approach to global ocean modeling. *Ocean Modelling*, *69*, 211–232. https://doi.org/10.1016/j.ocemod.2013.04.010

Rintoul, S. R., Hughes, C. W., & Olbers, D. (2001). The Antarctic Circumpolar Current system. In G. Siedler, J. Gould, & J. Church (Eds.), *Ocean circulation and climate* (1st ed., Vol. 103, pp. 271–301). Academic Press.

Saenz, J. A., Chen, Q., & Ringler, T. (2015). Prognostic residual mean flow in an ocean general circulation model and its relation to prognostic Eulerian mean flow. *Journal of Physical Oceanography*, *45*(9), 2247–2260. https://doi.org/10.1175/jpo-d-15-0024.1

Salmon, R. (1980). Baroclinic instability and geostrophic turbulence. *Geophysical & Astrophysical Fluid Dynamics*, *15*(1), 167–211. https://doi.org/10.1080/03091928008241178

Schopf, P. S., & Loughe, A. (1995). A reduced-gravity isopycnal ocean model: Hindcasts of El Niño. *Monthly Weather Review*, *123*(9), 2839–2863. https://doi.org/10.1175/1520-0493(1995)123⟨2839:ARGIOM⟩2.0.CO;2

Scott, R. B., & Wang, F. (2005). Direct evidence of an oceanic inverse kinetic energy cascade from satellite altimetry. *Journal of Physical Oceanography*, *35*(9), 1650–1666. https://doi.org/10.1175/JPO2771.1

Seland, Ø., Bentsen, M., Olivié, D., Toniazzo, T., Gjermundsen, A., Graff, L. S., et al. (2020). Overview of the Norwegian Earth System Model (NorESM2) and key climate response of CMIP6 DECK, historical, and scenario simulations. *Geoscientific Model Development*, *13*(12), 6165–6200. https://doi.org/10.5194/gmd-13-6165-2020

Skamarock, W. C. (2004). Evaluating mesoscale NWP models using kinetic energy spectra. *Monthly Weather Review*, *132*(12), 3019–3032. https://doi.org/10.1175/MWR2830.1

Smith, K. S., & Vallis, G. K. (2001). The scales and equilibration of midocean eddies: Freely evolving flow. *Journal of Physical Oceanography*, *31*(2), 554–570. https://doi.org/10.1175/1520-0485(2001)031⟨0554:TSAEOM⟩2.0.CO;2

Smith, R. D., & Gent, P. R. (2004). Anisotropic Gent–Mcwilliams parameterization for ocean models. *Journal of Physical Oceanography*, *34*(11), 2541–2564. https://doi.org/10.1175/jpo2613.1

Smith, R. D., & McWilliams, J. C. (2003). Anisotropic horizontal viscosity for ocean models. *Ocean Modelling*, *5*(2), 129–156. https://doi.org/10.1016/s1463-5003(02)00016-1

Soufflet, Y., Marchesiello, P., Lemarié, F., Jouanno, J., Capet, X., Debreu, L., & Benshila, R. (2016). On effective resolution in ocean models. *Ocean Modelling*, *98*, 36–50. https://doi.org/10.1016/j.ocemod.2015.12.004

Storer, B. A., Buzzicotti, M., Khatri, H., Griffies, S. M., & Aluie, H. (2022). Global energy spectrum of the general oceanic circulation. *Nature Communications*, *13*(1), 5314. https://doi.org/10.1038/s41467-022-33031-3

Tréguier, A.-M., Held, I., & Larichev, V. (1997). Parameterization of quasigeostrophic eddies in primitive equation ocean models. *Journal of Physical Oceanography*, *27*(4), 567–580. https://doi.org/10.1175/1520-0485(1997)027<0567:poqeip>2.0.co;2

Vallis, G. K. (2017). *Atmospheric and oceanic fluid dynamics: Fundamentals and large-scale circulation* (2nd ed., p. 946). Cambridge University Press.

Yankovsky, E., Zanna, L., & Smith, K. S. (2022). Influences of mesoscale ocean eddies on flow vertical structure in a resolution-based model hierarchy. *Journal of Advances in Modeling Earth Systems*, *14*(11), e2022MS003203. https://doi.org/10.1029/2022MS003203

Young, W. R. (2012). An exact thickness-weighted average formulation of the Boussinesq equations. *Journal of Physical Oceanography*, *42*(5), 692–707. https://doi.org/10.1175/JPO-D-11-0102.1

Zanna, L., Porta Mana, P., Anstey, J., David, T., & Bolton, T. (2017). Scale-aware deterministic and stochastic parametrizations of eddy-mean flow interaction. *Ocean Modelling*, *111*, 66–80. https://doi.org/10.1016/j.ocemod.2017.01.004

Zhao, R., & Vallis, G. (2008). Parameterizing mesoscale eddies with residual and Eulerian schemes, and a comparison with eddy-permitting models. *Ocean Modelling*, *23*(1), 1–12. https://doi.org/10.1016/j.ocemod.2008.02.005